Universiteit Antwerpen

This item is the archived peer-reviewed author-version of:

Atomically engineered interfaces yield extraordinary electrostriction

Reference:
Zhang Haiwu, Pryds Nini, Park Dae-Sung, Gauquelin Nicolas, Santucci Simone, Christensen Dennis, V., Jannis Daen, Chezganov Dmitry, Rata Diana A., Insinga Andrea R., ...- Atomically engineered interfaces yield extraordinary electrostriction
Nature - ISSN 1476-4687 - 609:7928(2022), p. 695-700
Full text (Publisher's DOI): https://doi.org/10.1038/S41586-022-05073-6
To cite this reference: https://hdl.handle.net/10067/1905760151162165141

uantwerpen.be
Institutional repository IRUA

Atomically engineered interfaces yield extraordinary electrostriction

Haiwu Zhang[1,7*], Nini Pryds[1,7*], Dae-Sung Park[2], Nicolas Gauquelin[3], Simone Santucci[1], Dennis V. Christensen[1], Daen Jannis[3], Dmitry Chezganov[3], Diana A. Rata[4], Andrea R. Insinga[1], Ivano E. Castelli[1], Johan Verbeeck[3], Igor Lubomirsky[5], Paul Muralt[6], Dragan Damjanovic[2], and Vincenzo Esposito[1*]

[1]Department of Energy Conversion and Storage, Technical University of Denmark, Fysikvej 309, 2800 Kgs. Lyngby, Denmark

[2]Group for Ferroelectrics and Functional Oxides, Institute of Materials, Swiss Federal Institute of Technology-EPFL, CH-1015 Lausanne, Switzerland

[3]Electron Microscopy for Materials Science (EMAT), University of Antwerp, B-2020 Antwerpen, Belgium

[4]Institut für Physik, Martin-Luther-Universität Halle-Wittenberg, 06120 Halle, Germany

[5]Department of Materials and Interfaces, Weizmann Institute of Science, Rehovot 76100, Israel

[6]Department of Materials, Swiss Federal Institute of Technology, 1015, Switzerland

[7] These authors contributed equally: H. Zhang, N. Pryds

*E-mail: haizh@dtu.dk; nipr@dtu.dk; vies@dtu.dk

Electrostriction is a property of the dielectric materials whereby an applied electric field induces a mechanical deformation proportional to the square of the electric field. The magnitude of the effect is usually minuscule (less than 10^{-19} m^2/V^2 for simple oxides). However, symmetry-breaking phenomena at the interfaces can offer

an efficient strategy to design new properties.[1, 2] Herein, we report an engineered electrostrictive effect via the epitaxial deposition of alternating layers of Gd_2O_3-doped CeO_2 and Er_2O_3-stabilized δ-Bi_2O_3 with atomically controlled interfaces on $NdGaO_3$ substrates. The value of the electrostriction coefficient achieved is 2.38 × 10^{-14} m^2/V^2, exceeding the best-known relaxor ferroelectrics by three orders of magnitude. Our theoretical calculations indicate that the extraordinary electrostriction arises from coherent strain imparted by the interfacial lattice discontinuity. These artificial heterostructures open a new avenue for designing and manipulating electrostrictive materials and devices for nano/micro actuation and cutting-edge sensors.

Materials that develop strains in response to an electric field have attracted substantial attention over the past decades owing to their wide applications, including non-resonant actuators, high-end transducers, artificial muscles, energy harvesting, and various sensors.[3, 4] Although piezoelectricity is limited to materials with a non-centrosymmetric crystal structure, electrostriction is a property exhibited by all dielectrics, which produces a high displacement accuracy in the absence of strain-field hysteresis and remnant polarisation. Electrostrictors are characterised by a fourth rank tensor called electrostriction coefficient (M_{ijmn}, here shortened as M_{xx}), which relates the induced strain (ε_{ij}^*) to the electric field (E_n) via $\varepsilon_{ij}^* = \sum_{n,m} M_{ijmn} E_n E_m$. The magnitude of M_{xx} is usually

low (<< 10^{-19} m^2/V^2) for simple oxides, such as MgO, TiO_2, and Y:ZrO_2.[5] Relaxor ferroelectrics and ferroelectric polymers are two archetypes of electrostrictive materials which exhibit high electromechanical responses.[5, 6] Lead-based relaxors exhibit a larger electrostriction coefficient (1.0×10^{-17} m^2/V^2) and generate high saturation stress (up to 150 MPa).[7, 8] Polymers also possess high electrostriction coefficients (1.8×10^{-18} m^2/V^2). However, the stress delivered is approximately two orders of magnitude lower (2 MPa on average).[9] Recently, Gd_2O_3-doped CeO_2 (CGO) based electrostriction materials revealed anomalously large electrostriction with the saturation stress exceeding 500 MPa.[10-14] This class of electrostrictors represents a promising lead-free alternative to ferroelectric materials.

The integration and size reduction of nano/microelectronic devices impetus the development of electrostrictors that can operate with low power consumption and long-term stability. Heterostructure multilayers are a promising platform for the development of next-generation nanoscale materials and properties, e.g., fast ionic conduction,[15] metal-to-insulator transitions,[16] and ferroelectricity in paraelectric materials.[17] Such properties are associated with the complex yet tailorable interfacial properties, resulting in ionic/electronic redistribution, symmetry breaking, and strain gradients.[1, 2, 18] However, the scaling effect associated with interface engineering of electrostriction materials remains a fundamental question needed to be addressed.[19-23]

Herein, we report a novel approach for engineering electrostriction through artificial interfaces. Gd_2O_3-doped CeO_2 (CGO) and Er_2O_3-stabilized δ-Bi_2O_3 (ESB) were selected to design multilayers as model material systems. The lattice mismatch between the CGO and the ESB layers was used to tune the local interfacial distortions and amplify the electrostriction. This strategy yields an electrostrictive enhancement of three orders of magnitude compared to single-layered CGO films, resulting in the highest value (M_{xx} ~10^{-14} m^2/V^2) measured in any electrostrictive materials. This kind of artificial electrostrictive heterostructures opens up new opportunities for developing high-performance nano-/micro-electromechanical devices.

Ultrathin films were deposited using pulsed laser deposition (PLD). The heterostructures contain alternating layers of gadolinium-doped ceria ($Ce_{0.8}Gd_{0.2}O_{1.9}$, CGO) and erbium-stabilised bismuth oxide ($Er_{0.4}Bi_{1.6}O_3$, ESB) deposited on pseudocubic (pc) [010]-oriented $NdGaO_3$ substrates (NGO). The heterostructures are defined as NGO/CGO/$[ESB/CGO]_N$, where N = 1, 3, 7, 10, 15 is the number of [ESB/CGO] bilayers schematically illustrated in Fig. 1a. The total thickness (d) of the thin films was fixed at approximately 17 nm with a CGO to ESB thickness ratio of 1:1. The modulation length (Λ) is the thickness of the [ESB/CGO] bilayers, which is related to d (the total thickness of the film) and N (the number of repetitions) via $\Lambda = d/(N+1/2)$; for N = 1, 3, 7, 10 and 15, the values of Λ are 11.33, 4.86, 2.27, 1.62, and 1.10 nm, respectively. The high-angle annular dark-field scanning transmission electron microscopy (HAADF-STEM) Z-

contrast images of NGO/CGO/[ESB/CGO]$_7$ reveal the epitaxial relationship between the constituent layers, with ESB exhibiting a brighter ADF image contrast than CGO (Fig. 1b). The atomically resolved energy-dispersive X-ray (EDX) profiles of Ce, Er, and O exhibit the compositional variation that enables the identification of well-defined interfaces. Dopant segregation or formation of extended defects (e.g., dislocations or line defects) is not observed down to Λ = 2.27 nm; however, a further decrease in Λ to 1.62 nm results in substantial chemical intermixing, as demonstrated by the electron energy loss spectroscopy (EELS) and STEM-EDX results (Extended Data Fig. 1).

The electrostrictive response of the heterostructure is proportional to the square of the electric field strength (Extended Data Fig. 2). The generated stress exceeds 9.7 GPa at the maximum applied electric field of 17.4 kV/cm. Fig. 1c shows the electrostriction coefficient (M_{xx}) of the heterostructure as a function of Λ measured at 1 Hz. For ease of comparison, the M_{xx} of a single layer of CGO thin film has been plotted along with the reported coefficient values for CGO films of varying thickness ($d \geq 400$ nm).[10, 12-14] For single-layered films, Λ is equal to the film thickness (d). A comparison with Bi_2O_3-based films is not included as their electrostrictive properties have not yet been investigated owing to their structural and chemical instabilities.[11, 24, 25] As seen in Fig. 1c, the plot of the measured M_{xx} exhibits a "volcano-like" shape as a function of $1/\Lambda$, with the maximum value measured at Λ = 2.27 nm. The electrostriction coefficient increases linearly as $1/\Lambda$ increases up to 0.44 nm^{-1}. This configuration corresponds to 7 bilayers of [ESB/CGO].

Further increases of $1/\Lambda$ beyond 0.44 nm^{-1} lead to a decrease in the electrostriction coefficient. The initial linearly increasing values align well with the reported M_{xx} values for CGO, regardless of the deposition method, process parameters, film microstructure, and type of substrate/electrode.[10, 12-14] Remarkably, the maximum M_{xx} of the heterostructure (2.38×10^{-14} m^2/V^2) is more than three orders of magnitude greater than those of thick CGO films.[10, 12-14] However, as Λ decreases below $\Lambda = 1.62$ nm ($N > 7$), the electrostriction coefficient decreases substantially, which can be attributed to intermixing at the interfaces (Extended Data Fig. 1) that results in deteriorated electrostriction.

The chemical stability and the electromechanical performance of heterostructures with different stacking sequences were also investigated (Extended Data Fig. 3). When ESB was deposited directly onto NGO (NGO/ESB/$[CGO/ESB]_3$), the heterostructure exhibited a reduced electrostriction coefficient of 3.0×10^{-16} m^2/V^2 (Extended Data Fig. 3). By contrast, when CGO was deposited onto NGO (NGO/CGO/$[ESB/CGO]_3$), the heterostructure exhibited chemical stability with substantially enhanced electrostriction, highlighting the importance of the stacking sequence. Therefore, we have used the NGO/CGO/$[ESB/CGO]_N$ as the main configuration for our experiments, where the heterostructure is capped with CGO to prevent the degradation of the ESB layer. Fig. 1d shows the plots of M_{xx} for heterostructures with $\Lambda = 11.33$, 2.27, and 1.10 nm as a function of frequency. The performance of the heterostructures is superior to that of reported

123 individual electrostrictive materials, including bulk CGO,[26] Y/Nb:Bi_2O_3,[11] $La_2Mo_2O_9$,[27]
124 Y:ZrO_2 (YSZ)[11], or commercial relaxor ferroelectrics, such as $Pb(Mg_{1/3}Nb_{2/3})O_3$-$PbTiO_3$
125 (PMN-PT),[6] P(VDF-TrFE) copolymers[9]. The electrostriction of the heterostructures also
126 surpasses the recently discovered ultrahigh electrostriction of lead halide perovskites.[28]
127 Similar to bulk CGO, the measured M_{xx} of the heterostructures decreases with an increase
128 in frequency ($1 \leq f \leq 200$ Hz): for $\Lambda = 2.27$ nm, it decreases from 2.38×10^{-14} m^2/V^2 at 1
129 Hz to 3.76×10^{-15} m^2/V^2 at 200 Hz. This enhanced electrostrictive response can be used
130 in novel applications. It reduces the operating electric field substantially, improving the
131 long-term stability of the devices and lowering their energy consumption.
132 A potential drawback of multilayers is the possible delamination at the interfaces after
133 cyclic electrical loading, which could lead to the failure of the electrostrictive devices.
134 Therefore, the fatigue behaviour of the NGO/CGO/$[ESB/CGO]_7$ heterostructure was
135 investigated as a function of time by applying a sinusoidal electric field with a constant
136 amplitude of 17.4 kV/cm at different frequencies (Extended Data Fig. 4). Notably, the
137 heterostructure remained electromechanically active, and the field-induced stress did not
138 degrade after 1000 cycles at 1 Hz. The electromechanical stability was further confirmed
139 by subsequent measurements at 50 and 200 Hz for another 1000 cycles (Extended Data
140 Fig. 4).
141 Fig. 2a shows the X-ray diffraction (XRD) reciprocal space mapping (RSM) analysis for
142 the heterostructures around the asymmetric $(221)_{pc}$ reflection of NGO. The out-of-plane

position and shape of the (420) reflections of the heterostructures vary with a decrease in Λ. The overall structural coherency is maintained, indicating that the in-plane lattice parameters of the heterostructure are coherent with respect to the substrate. This result is consistent with the scanning transmission electron microscopy (STEM) results. The sub-peaks along the out-of-plane direction observed for Λ = 11.33 and 4.86 nm are attributed to the lattice relaxations within the CGO and ESB layer. The XRD (2θ-ω scan) analysis indicates that the heterostructures are phase-pure films oriented along the (110) crystallographic direction (Fig. 2b). The Laue diffraction oscillations around the superlattice peaks indicate that the periodicity of the fluorite lattice is well preserved for different modulation lengths.

The fluorite oxides (CGO and ESB) grow epitaxially on the perovskite oxide (NGO) with a rotation of 45° to account for the substantial mismatch and allow cube-on-cube growth. This arrangement results in an epitaxial relationship of $<110>_{CGO}//<010>_{pc\ NGO}$ such that the mismatch is reduced to ~1% (see Fig. 2c and Extended Data Fig. 1a).

The lattice mismatch between the heterostructure and the substrate is compensated completely by the elastic strain, generating an average in-plane strain of 1% in the film (see Fig. 2d and Supplementary Fig. 1). In contrast, the magnitude of the average out-of-plane compressive strain decreases from ca. 1.5% to ca. 1% when Λ is decreased from 11.33 to 2.27 (N increased from 1 to 7). Consequently, the volumetric strain ($\Delta V/V$) increases from 0.48% to 0.99%, with Λ = 2.27 nm being the largest. The abnormal change

in strain for $\Lambda < 2.27$ nm is attributed to the chemical intermixing at the interfaces, as shown in the EELS and EDX maps shown in Extended Data Fig. 1b and c. The variation of out-of-plane strain (and hence $\Delta V/V$) as a function of Λ correlates well with the measured electrostriction coefficient (Fig. 1c).

Based on the structural analysis discussed above, we employed atomic-scale simulations on heterostructures with alternating layers of CGO and ESB to investigate the structural evolution as a function of Λ. The simulations were performed by fixing the composition to the experimental stoichiometry, i.e., $Ce_{0.8}Gd_{0.2}O_{1.9}$ and $Er_{0.4}Bi_{1.6}O_3$, respectively. The model structures were optimised with the in-plane lattice parameters fixed to the NGO substrate, while the out-of-plane lattice parameter was allowed to relax. The calculations were performed for heterostructures with different modulation lengths, i.e., 96, 48, 32, 24, 16, 12, 8, 6, and 4 cationic planes, respectively. Fig. 3a shows a schematic illustration of the modulation length, and the definition of the cationic interplanar distance (d_C) projected in the out-of-plane direction. The amplitude of the lattice distortion at the CGO/ESB interfaces was calculated based on the variation in d_C as a function of Λ (Fig. 3b). For example, for $\Lambda = 18.56$ nm (96 cationic planes), the lattice relaxation yields two distinct plateaus at 1.92 and 1.96 Å, close to the individual interplanar distances of bulk CGO and ESB, respectively. This range of values agrees well with the lattice relaxation observed for $\Lambda = 11.33$ and 4.86 nm ($N = 1$ and 3) in the RSMs shown in Fig. 2a.

182 The effect of the interfaces becomes progressively evident with a decrease in Λ. The
183 interplanar distances become gradually frustrated with a reduction in Λ down to 2.33 nm
184 and beyond (approaching Λ = 2.27 nm for NGO/CGO[ESB/CGO]$_7$). At Λ = 0.78 nm, it
185 is difficult to distinguish between the interfaces and individual regions, indicating that
186 CGO and ESB adopt similar lattice parameters.
187 We further evaluate the role of modulation length on electrostriction by two different
188 models: (1) A phenomenological model considering elastic and electric dipoles and (2)
189 molecular dynamics (MD) simulations. For the former case, we consider an ensemble of
190 elastic dipoles, where each is coupled to an electric dipole, as schematically illustrated in
191 the inset in Fig. 4a. The elastic-electric dipoles interact with an external electric field by
192 changing their orientation in space (Supplementary Information "Phenomenological
193 Simulation" section). M_{xx} is then calculated as a function of volumetric strain ($\Delta V/V$) to
194 mimic the strain state of the heterostructures as a result of the evolution of modulation
195 length. Fig. 4a shows that the calculated M_{xx} increases fast with the increase of $\Delta V/V$,
196 which is in agreement with the experimental observation of increasing lattice parameter
197 for increasing $1/\Lambda$ up to 0.5 nm^{-1} (Fig. 3c), and the increase of M_{xx} in the same value range
198 of $1/\Lambda$ (Fig. 1c).
199 We further employed MD simulations to investigate the effect of Λ on electrostriction.
200 We apply an external electric field on the heterostructures, allowing the lattice parameters

201 (*a*/*b*/*c*) to relax (see Extended data Fig. 5). The results confirmed that the field-induced
202 strain exhibits a "volcano-like" shape as a function of Λ (Fig. 4b).
203 To explore the applicability of multilayering for engineering electrostriction, we have
204 further investigated the field-induced strain as a function of Λ with different defective
205 oxide structures (fluorite, perovskite, garnet, and spinel). These results are fully consistent
206 with the "volcano-like" behaviour, demonstrating that interfacial engineering is a
207 promising strategy to achieve large electrostriction (Extended data Fig. 6).
208 Here, we propose that the volumetric strain change in the heterostructure is associated
209 with substantial variation of the local distortions, leading to the coexistence of energy-
210 competing elastic dipoles (and hence electric dipoles). A radial distribution function
211 (RDF) analysis confirms this behaviour: decreasing Λ, the radial distribution broadens,
212 indicating that the distances between the cations and the anions in the heterostructures
213 increase (see Extended data Fig. 7 and 8). We conclude that, in the strained multilayers
214 (without external electric field), the ions are not fixed to high-symmetry positions, gaining
215 thus in spatial freedom and thus increasing elastic and electrostatic energy
216 (Supplementary Information Fig. 2). When an electric field is applied, the electric dipoles,
217 which are coupled to elastic dipoles, are easier to polarise.[29, 30] They are then able to adjust
218 their relative positions, leading to larger M_{xx}. This effect becomes even more pronounced
219 when decreasing Λ, owing to the increase in the strength of the elastic dipoles. However,
220 for Λ beyond a certain value, the oxygen sublattice becomes disordered, and the

volumetric strain effect is lost (Fig. 3c), thus resulting in the decrease of electrostriction. In short, the reduction in the modulation length Λ plays a two-fold role: a) it increases the strength of the elastic dipoles, and b) it leads to the coexistence of energy-competing elastic dipoles, which are easier to switch between different directions in response to the external electric field. Fig. 4c illustrates the mechanism schematically.

In conclusion, we show that the electrostriction effect can be designed and manipulated by artificial heterostructures. This framework provides new insights into the role of interfacial strain discontinuities, which can be further extended to other defective oxide systems. Such strain modulation results in the displacement of ions away from the ideal lattice sites. It provides the degree of freedom required to control the strength of the elastic dipoles and their ability to reorient, which is a key reason for achieving a large electrostriction coefficient in ultrathin heterostructures. These factors are a prerequisite for replacing lead-based piezoelectric materials (such as commercial PMN-PT) with environment-friendly and non-toxic electrostrictors with superior, reliable, and optimised properties, making them suitable for a wide range of applications, including optical communication, biomedical actuation, and micro-sensors.

Online content

Any methods, additional references, Nature Research reporting summaries, source data, extended data, supplementary information, acknowledgements, peer review information,

details of author contributions and competing interests, and statements of data and code availability are available at http://npg.nature.com.

1. Ramesh, R. & Schlom, D. G. Creating emergent phenomena in oxide superlattices. *Nat. Rev. Mater*. **4**, 257-268 (2019).

2. Yang, M. M. et al. Piezoelectric and pyroelectric effects induced by the interface polar symmetry. *Nature* **584**, 377-381 (2020).

3. Li, F., Jin, L., Xu, Z., Zhang, S. Electrostrictive effect in ferroelectrics: An alternative approach to improve piezoelectricity. *Appl. Phys. Rev*. **1**, 011103 (2014).

4. Lehmann, W. et al. Giant lateral electrostriction in ferroelectric liquid-crystalline elastomers. *Nature* **410**, 447-450 (2001).

5. Yimnirun, R., Moses, P. J., Newnham, R. E. & Meyer Jr, R. J. Electrostrictive strain in low-permittivity dielectrics. *J. Electroceram*. **8**, 87-98 (2002).

6. Li, F., Jin, L., Xu, Z., Wang, D. & Zhang, S. Electrostrictive effect in $Pb(Mg_{1/3}Nb_{2/3})O_3$-$xPbTiO_3$ crystals. *Appl. Phys. Lett*. **102**, 152910 (2013).

7. Zednik, R. J., Varatharajan, A., Oliver, M., Valanoor, N. & McIntyre, P. C. Mobile ferroelastic domain walls in nanocrystalline PZT films: The direct piezoelectric effect. *Adv. Funct. Mater*. **21**, 3104-3110 (2011).

8. Li, F. et al. Ultra-high piezoelectricity in ferroelectric ceramics by design. *Nat. Mater*. **17**, 349-354 (2018).

9. Zhang, Q. M., Bharti, V. & Zhao, X. Giant electrostriction and relaxor ferroelectric behaviour in electron-irradiated poly(vinylidene fluoride-trifluoroethylene) copolymer. *Science* **280**, 2101-2104 (1998).

10. Korobko, R. et al. Giant electrostriction in Gd-doped ceria. *Adv. Mater*. **24**, 5857-5861 (2012).

11. Yavo, N. et al. Large nonclassical electrostriction in (Y, Nb)-stabilised δ-Bi_2O_3. *Adv. Funct. Mater*. **26**, 1138-1142 (2016).

12. Korobko, R. et al. In situ extended X-ray absorption fine structure study of electrostriction in Gd-doped ceria. *Appl. Phys. Lett*. **106**, 042904 (2015).

13. Hadad, M., Ashraf, H., Mohanty, G., Sandu, C. & Muralt, P. Key-features in processing and microstructure for achieving giant electrostriction in gadolinium-doped ceria thin films. *Acta Mater*. **118**, 1-7 (2016).

14. Santucci, S., Zhang, H., Sanna, S., Pryds, N. & Esposito, V. Enhanced electromechanical coupling of TiN/$Ce_{0.8}Gd_{0.2}O_{1.9}$ thin film electrostrictor. *APL Mater*. **7**, 071104 (2019).

15. Sata, N., Eberman, K., Eberl, K., & Maier, J. Mesoscopic fast ion conduction in nanometer-scale planar heterostructures. *Nature* **408**, 946-949 (2000).

16. Domínguez, C. et al. Length scales of interfacial coupling between metal and insulator phases in oxides. *Nat. Mater*. **19**, 1182-1187 (2020).

17. Haeni, J. H. et al. Room-temperature ferroelectricity in strained $SrTiO_3$. Nature **430**, 758-761 (2004).

18. Cancellieri, C. et al. Electrostriction at $LaAlO_3$/$SrTiO_3$ interface. *Phys. Rev. Lett*. **107**, 056102 (2011).

19. Junquera, J. & Ghosez, P. Critical thickness for ferroelectricity in perovskite ultrathin films. *Nature* **422**, 506-509 (2003).

20. Fong, D. D. et al. Ferroelectricity in ultrathin perovskite films. *Science* **304**, 1650-1653 (2004).

21. Mani, B. K., Chang, C. M., Lisenkov, S. & Ponomareva, I. Critical Thickness for Antiferroelectricity in $PbZrO_3$. *Phys. Rev. Lett*. **115**, 097601 (2015).

22. Zhang, W. & Ouyang, J. Interface engineering of ferroelectric thin heterostructures. Nanostructures in ferroelectric films for energy applications include domains, grains, interfaces, and engineering methods (Elsevier Inc., 2019). doi:10.1016/B978-0-12-813856-4.00006-5.

23. Ji, D. et al. Freestanding crystalline oxide perovskites down to monolayer limit *Nature* **570**, 87-90 (2019).

24. Sanna, S. et al. Enhancement of chemical stability in confined δ-Bi_2O_3. *Nat. Mater*. **14**, 500-504 (2015).

25. Sanna, S. et al. Structural instability and electrical properties of epitaxial Er_2O_3-stabilized Bi_2O_3 thin films. *Solid State Ionics*. **266**, 13-18 (2014).

26. Varenik, M. et al. Dopant concentration controls the quasi-static electrostrictive strain response of ceria ceramics. *ACS Appl. Mater. Interfaces*. **12**, 39381-39387 (2020).

27. Li, Q. et al. Giant thermally enhanced electrostriction and polar surface phases in $La_2Mo_2O_9$ oxygen ion conductors. *Phys. Rev. Materials*. **2**, 041403(R) (2018).

28. Chen, B. et al. Large electrostrictive responses in lead halide perovskites. *Nat. Mater*. **17**, 1020-1026 (2018).

29. Das, T. et al. Anisotropic chemical strain in cubic ceria due to oxygen-vacancy-induced elastic dipoles. *Phys. Chem. Chem. Phys*. **20**, 15293-15299 (2018).

30. Kraynis, O. et al. Modeling Strain Distribution at the Atomic Level in Doped Ceria Films with Extended X-ray Absorption Fine Structure Spectroscopy. *Inorg. Chem*. **58**, 7527-7536 (2019).

Acknowledgements

This research was supported by the BioWings project funded by the European Union's Horizon 2020, Future and Emerging Technologies (FET) programme (Grant No. 801267) and the Danish Council for Independent Research Technology and Production Sciences for the DFF- Research Project 2 (Grant No. 48293). N.P. and D.V.C. acknowledge funding from Villum Fonden for the NEED project (00027993) and the Danish Council for Independent Research Technology and Production Sciences for the DFF- Research Project 3 (Grant No 00069 B). V.E. acknowledges funding from Villum Fonden for the IRIDE project (00022862). N.G. and J.V. acknowledge funding from the GOA project ("Solarpaint") of the University of Antwerp. The microscope used in this work was partly funded by the Hercules Fund from the Flemish Government. D.J. acknowledges funding from the FWO Project G093417N from the Flemish Fund for Scientific Research. D.C. acknowledges the TOP/BOF funding of the University of Antwerp. This project has received funding from the European Union's Horizon 2020 Research Infrastructure - Integrating Activities for Advanced Communities under grant agreement No 823717-ESTEEM3. The authors would like to thank Thierry Désiré Pomar and Achilles John Bergne for English proofreading.

Author Contributions

H. Z., N. P., and V. E. conceived the idea and designed the project. H.Z. and S.S. prepared the samples and characterised their electromechanical properties. N.G. performed STEM measurements and analysed the STEM-EELS results. D.J. assisted with the processing of the HAADF-STEM data analysis, and D.C. performed the statistical analysis of the EDX results under the supervision of N.G. and J.V. D.P., P.M., D. D. and R.D. performed the XRD and RSM characterisation. H. Z., I. L. and I. E. C. performed atomic-scale simulations and analysis. D. V. C. performed finite element simulations. A. R. I., I. L. and P. M. developed the analytical model. H.Z., V.E. and N.P. wrote the manuscript with input from all the authors. All authors have read and agreed to the published version of the manuscript.

Competing interests The authors declare no competing financial interests.

Additional information

Supplementary information is available for this paper at www.nature.com.

Correspondence and requests for materials should be addressed to H. Z., V. E., and N. P.

Reprints and permissions information is available online at http://npg.nature.com/reprintsandpermissions.

Methods

Thin-film fabrication. The heterostructures were fabricated by alternating CGO and ESB layers using PLD with a multi-target carousel. The target–substrate distance was 50 mm. The 248 nm KrF excimer laser was operated at 2 Hz with a laser fluence of 1.8 J cm^{-2}. The deposition rate was ~0.05 Å per pulse. The total number of laser shots on the targets were 3560 (1780 for CGO and 1780 for ESB), yielding a total thickness of ~17

nm. The ratio of CGO to ESB was fixed at 1:1, whereas the thickness of each layer varied with the modulation length. The deposition was performed at 600 °C at an oxygen partial pressure of 10^{-3} mbar. The heating/cooling rate was 10 °C/min. The Au top electrodes were sputtered with a Bal-Tec SCD 005 sputter coater at room temperature.

STEM, EDX, and EELS measurements The cross-sectional transmission electron microscopy (TEM) lamellae were prepared via focused ion beam using an FEI HELIOS 650 dual-beam focused ion beam device. Carbon and platinum protective layers were deposited on the top of the film during the preparation process. The aberration-corrected HAADF-STEM and EDX were performed using a probe aberration-corrected 'cubed' FEI TITAN 80-300 electron microscope operated at 300 kV equipped with SUPER-X EDX detector system. Line profiles of the elemental distribution along the TEM lamellae were averaged over several unit cells laterally for better statistical analysis. The EELS data were acquired on a double aberration-corrected 'cubed' FEI-TITAN 80-300 electron microscope operated at 120 kV in monochromatic mode, providing an energy resolution of 150 meV.

XRD and RSMs analysis. The crystal structure and strain states were characterised using a high-resolution Bruker D8 discover diffractometer with monochromatic Cu $K_{\alpha}1$ radiation (λ = 1.5406 Å). Reciprocal space mapping was performed around the (221) asymmetric reflection of the NGO substrate.

Electrostriction measurements The electrostriction properties of the heterostructures were measured using a planar electrode configuration, with the two electrodes placed on top of the thin films in parallel (inset in Fig. 1c). The sinusoidal electric field was generated using an AIM-TTI TGP 3100 function generator, amplified by a Trek 2220

amplifier. The deflection at the free end of the cantilever was measured using a single-beam laser interferometer SIOS NA analyser at the second harmonic of the electrical field. An Ametek 7230 DSP lock-in amplifier was used to improve the signal-to-noise ratio (down to 0.2 nm). Additional details can be found in Supplementary Fig. 3. The electric field distribution within the cantilever was modelled using the finite element simulations, as shown in Supplementary Fig. 4.

Atomic-scale Simulations Atomic-scale simulations were performed based on the Born model of ionic solids.[31] This approach has been used extensively to model the effect of an electric field for various material systems, such as polarisation-electric field hysteresis and electro-strain hysteresis of ferroelectrics,[32] caloric effects of $MAPbI_3$,[33] and mobility of oxygen ions in CeO_2.[34] The ions are treated as classical particles, whereas the interatomic interactions are described by

$$V_{ij} = \frac{Z_i Z_j}{4\pi\varepsilon_0 r_{ij}} + A_{ij}\exp\left(-\frac{r_{ij}}{\rho_{ij}}\right) - \frac{C_{ij}}{r_{ij}^6} \quad (1)$$

where the first term describes the long-range Coulomb interactions and the following two terms correspond to the short-range electron cloud overlap and dispersion, respectively. The parameters r_{ij}, $Z_{i(j)}$, and ε_0 correspond to the distance between ions i and j, the valences of the ions, and the permittivity of free space, respectively;

During the simulation of the structural evolution as a function of Λ (Fig. 3 and Extended data Figure 7), the in-plane lattice parameters were kept fixed, whereas the out-of-plane lattice parameters were free to relax. For the calculation of the electrostriction

coefficient, the in-plane and out-of-plane lattice parameters were free to relax in response to the electric field (Fig. 4b and Extended data Figs. 5 and 6). Extended Data Fig. 8 shows a schematic illustration of the elastic dipoles resulting from local lattice distortions. During the simulations, the temperature was monitored using a Nosé–Hoover thermostat,[35, 36] as implemented in the LAMMPS package.[37] More details about the empirical Buckingham parameters and the supercell configurations can be found in Supplementary Fig. 4 and the related text.

Phenomenological simulations This model considered an ensemble of elastic dipoles, each elastic rigidly connected to an electric dipole. The elastic-electric dipoles were assumed to interact with an initial strain field and external electric field by changing their orientation in space. The equilibrium orientation was obtained by minimizing the sum of the total energy (E_{total}) of the system:

$$E_{\text{total}} = E_{\text{elastic}} + E_{\text{electric}} \quad (2)$$

where E_{elastic} and E_{electric} are the elastic and electric contributions, respectively. The effect of modulation length was captured by calculating the electrostriction coefficient as a function of the volumetric strain ($\Delta V/V$), which varied as a result of the modulation length change. More details about the interactions between the elastic and electric dipoles and their response to the external field can be found in Supplementary Fig. 5 and the related text.

Data Availability

The data supporting this study's findings are available from the corresponding authors upon reasonable request.

Code Availability

The code used for the creation of physical model and atomic-scale models are available from the corresponding authors upon reasonable request.

31. Born, M. and Mayer, J. E. Zur gittertheorie der ionenkristalle, *Z. Phys*. **75**, 1 (1932).

32. Chapman, J. B. J., Cohen, R. E., Kimmel, A. V. and Duffy, M. D. Improving the functional control of aged ferroelectrics using insights from atomistic modeling, *Phys. Rev. Lett*. **119**, 177602 (2017).

33. Liu, S. and Cohen, R. E. Response of methylammonium lead iodide to external stimuli and caloric effects from molecular dynamics simulations, *J. Phys. Chem. C*. **120**, 17274-17281 (2016).

34. Genreith-Schriever, A. and De Souza, R. A. Field-enhanced ion transport in solids: Reexamination with molecular dynamics simulations, *Phys. Rev. B*. **94**, 224304 (2016);

35. Nosé, S. A unified formulation of the constant temperature molecular dynamics methods. *J. Chem. Phys*. **81**, 511-519 (1984).

36. William G. Hoover. Canonical dynamics: Equilibrium phase-space distributions William. *Phys. Rev. A*. **31**, 1695-1697 (1985).

37. Plimpton, S. Fast Parallel Algorithms for Short-Range Molecular Dynamics. *J. Comput. Phys*. **117**, 1-19 (1995).

Figure legends:

Figure 1

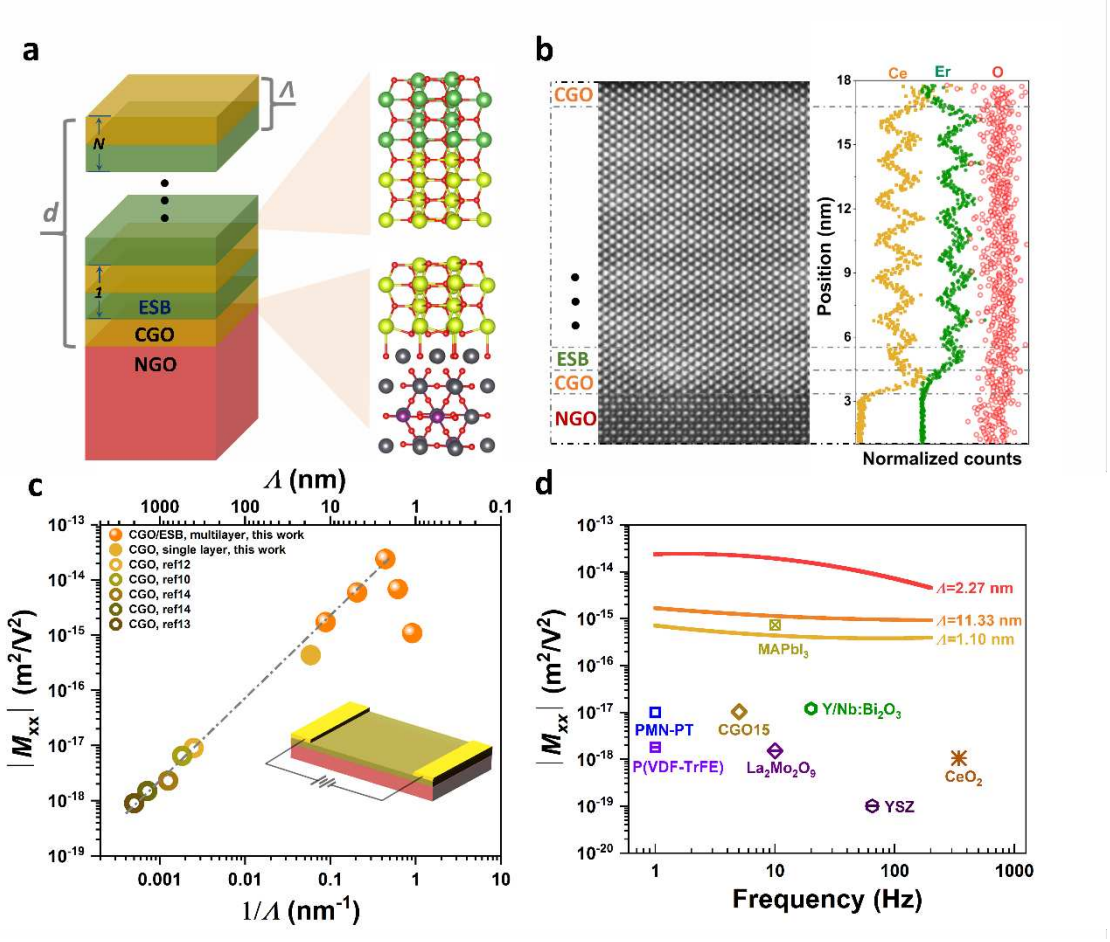

Fig. 1| Multilayer structure and electrostrictive property of NGO/CGO/[ESB/CGO]$_N$. a, Schematic illustration of the multilayer architecture. **b**, HAADF-STEM image and EDX compositional variations for Λ = 2.27 nm. **c**, Electrostriction coefficient (M_{xx}) as a function of modulation length (Λ) measured at 1 Hz. The inset schematically illustrates the top-top electrode configuration. **d**, Electrostriction coefficient (M_{xx}) as a function of frequency for heterostructures with Λ = 11.33, 2.27, and 1.10 nm. Electrostriction properties of various electrostrictive materials are shown for comparison: CeO_2,[26] CGO15,[26] Y/Nb:Bi_2O_3,[11] YSZ,[11] $La_2Mo_2O_9$,[27] PMN-PT,[6] P(VDF-TrFE),[9] and $MAPbI_3$.[28]

Figure 2

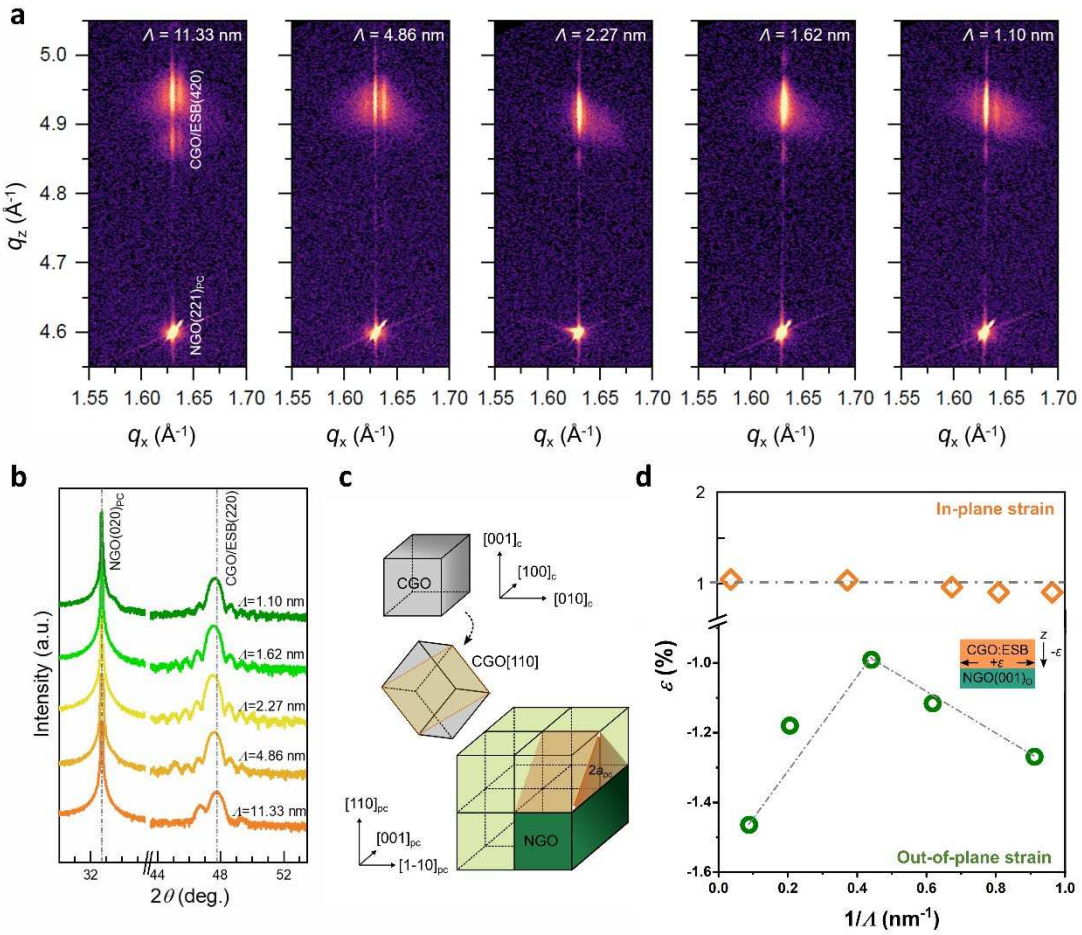

Fig. 2| Structural analysis of NGO/CGO/[ESB/CGO]$_N$. **a**, Reciprocal space mappings (RSMs) of the NGO/CGO/[ESB/CGO]$_N$ heterostructures around the asymmetric $(221)_{pc}$ reflection of the NGO substrate. **b**, X-ray diffraction pattern (2θ-ω scans) of the films. **c**, Schematic illustration of the epitaxial relationship between the heterostructure and the NGO substrate. **d**, Evolution of the in-plane and out-of-plane strains. The in-plane and out-of-plane strains are calculated based on the RSMs and 2θ-ω scans, respectively. The error bars in **d** represent the fitting error of the lattice constants.

Figure 3

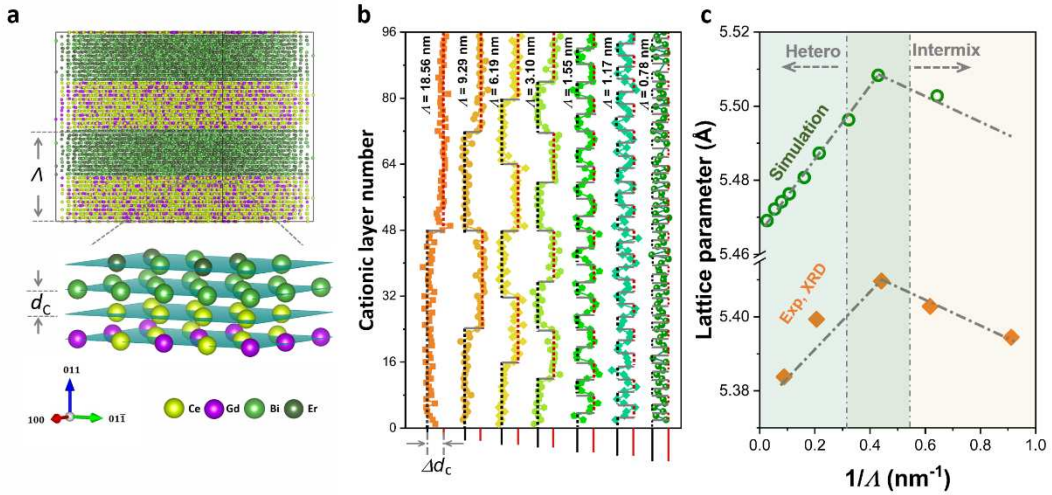

Fig. 3| Mechanism of interlayer interaction. **a**, Schematic illustration of the modulation length (Λ) and the cationic interplanar distance (d_C) for the heterostructures. The oxygen ions are omitted for clarity. **b**, Variation of d_C as a function of Λ projected onto the out-of-plane direction. The dark and red dot lines represent the individual interplanar distances of CGO (1.92 Å) and ESB (1.96 Å), respectively. Δd_C is 0.04 Å. **c**, Variation of the out-of-plane lattice parameters as a function of $1/\Lambda$. The dash-dotted lines are included as a guide to the eye only.

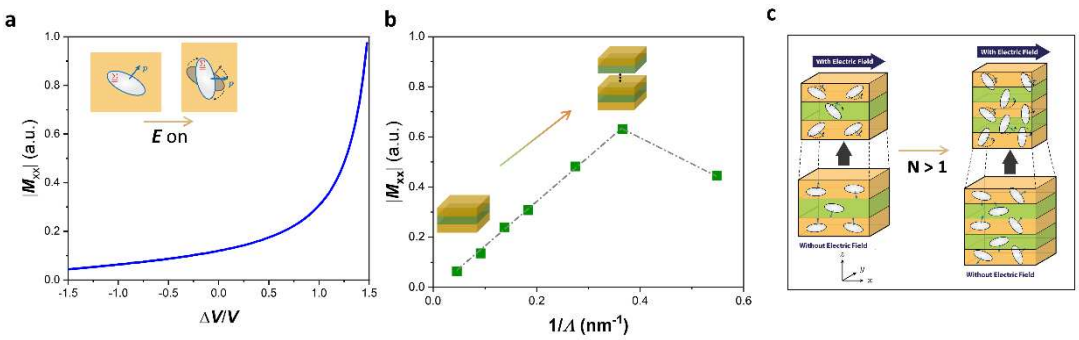

Figure 4

Fig. 4| Mechanism of the enhanced electrostriction. **a**, Electrostriction coefficient as a function of volumetric strain. The inset is a schematic illustration of the coupling between the electric dipole and elastic dipole, where $\overline{\overline{\Sigma}}$, p, ε, and E denote elastic dipole, electric dipole, strain field and electric field, respectively. **b**, Electrostriction coefficient as a function of modulation length. **c**, Schematical illustration of the mechanism showing the distribution and reorientation of elastic dipoles within heterostructures with different modulation lengths with and without external electric field.

Extended Data Figure legends:

Extended Data Figure 1 | STEM analysis of the heterostructures. a. HAADF-STEM images for NGO/CGO[ESB/CGO]$_{10}$ viewed along the [110] and [001] directions of the substrate from left to right, respectively. **b**. STEM-EELS compositional maps. For each sample, the leftmost image is the HAADF signal acquired simultaneously with the EELS measurement, followed by cerium $M_{4,5}$ in red, erbium $M_{4,5}$ in yellow, and neodymium $M_{4,5}$ in green (colour code: Ce: red; Er: yellow, Nd: green). **c**. STEM-EDX compositional maps.

Extended Data Figure 2 | Electrostriction Measurements a. Electrostrictive response of NGO/CGO/[ESB/CGO]$_7$ under an alternating electric field. The strain developed at the second harmonic of the applied electric field. **b**. Field-induced stress as a function of the electrical field for NGO/CGO/[ESB/CGO]$_N$ measured at 1 Hz. The field-induced stress increases linearly with an increase in the squared electric field. No saturation was observed within the measured electric field range, regardless of the modulation length. The dash-dotted lines represent linear fittings of the measured results.

Extended Data Figure 3 | Electrostriction measurements for heterostructures with different stacking sequences. Comparison of electrostriction coefficients for thick CGO films and bulk materials Multilayer* denotes NGO(100)/ESB/CGO/…/CGO, where ESB was deposited as the first layer.

Extended Data Figure 4 | Fatigue measurements. Electromechanical response of NGO/CGO/[ESB/CGO]$_7$ as a function of time. **a**. Electric field. **b.** Electromechanical stress in response to an electric field at 1 Hz **c**. Electromechanical stress as a function of the measured cycles at 1, 50, and 200 Hz. All measurements were performed by applying a sinusoidal electric field with a constant amplitude of 17.4 kV/cm.

Extended Data Figure 5 | Calculated field-induced strains in different directions. a. CGO20; **b**. ESB20; **c**. heterostructure (Λ = 2.33 nm). An electrical field was applied along the (100)-crystallographic direction. All lattice parameters were allowed to relax during the application of the electrical field. ε_{xx}, ε_{xy}, and ε_{xz} denote the strain developed along *the X*-, *Y*-, and *Z*-axis, respectively when the electric field is applied along with the *X*-axis. The Cartesian axes *X*, *Y*, and *Z* correspond to the (100), (01-1) and (011) crystallographic directions, respectively. Note that the lattices of CGO20, ESB20, and the heterostructure exhibit similar deformation in response to an electric field, that is, contract along the (100)-crystallographic direction and expand along with the (011) and (01-1)-crystallographic directions.

Extended Data Figure 6 | Electrostriction as a function modulation length for heterostructures with different crystal structures. **a**. fluorite: CGO20/YSZ8; **b**. perovskite: SFTO10/BYZO10; **c**. garnet: GGMO10/LSFO10; **d**. spinel: MGMO10/ZAZO10. The chemical formula for YSZ8, SFTO10, BYZO10, GGMO10, LSFO10, MGMO10 and ZAZO10 are $(Zr^{4+}_{0.92}Y^{3+}_{0.08})O^{2-}_{1.96}$, $Sr^{2+}_{1.0}(Fe^{3+}_{0.1}Ti^{4+}_{0.9})O^{2-}_{2.95}$, $Ba^{2+}_{1.0}(Y^{3+}_{0.1}Zr^{4+}_{0.9})O^{2-}_{2.95}$, $Gd^{3+}_{3.0}(Ga^{3+}_{4.5}Mg^{2+}_{0.5})O^{2-}_{11.75}$, $(La^{3+}_{2.5}Sr^{2+}_{0.5})Fe^{3+}_{5.0}O^{2-}_{11.75}$, $Mg^{2+}_{1.0}(Ga^{3+}_{1.8}Mg^{2+}_{0.2})O^{2-}_{3.90}$, $Zn^{2+}_{1.0}(Al^{3+}_{1.8}Zn^{2+}_{0.2})O^{2-}_{3.90}$, respectively. The defects are generated at random within the heterostructures. The insets schematically show the unit cell of the ideal structure. All the lattice parameters are allowed to relax during the application of the electrical field. Note that the optimal modulation length yielding maximized electrostriction coefficient (M_{xx}) is material dependent.

Extended Data Figure 7 | Ion distribution within the heterostructures. Radial distribution function of heterostructures as a function of modulation length (Λ). The first, second, and third peaks correspond to the cation–anion, anion–anion, and cation–cation distances, respectively. No electric field was applied.

Extended Data Figure 8 | Mechanism of elastic dipole and electric dipole formation. a. An ideal tetrahedron with cations having equivalent distances and three *C2* symmetry axes present. Schematic illustration of the elastic dipole

formation resulting from tetrahedral deformation along the **b**. (100), **c**. (010), and **d**. (001) directions. The off-site displacements of the cations result in local-symmetry breaking. Note that replacing one of the ions with Gd will result in a structure with three variants that are equivalent to the distortion of Ceria without Gd.

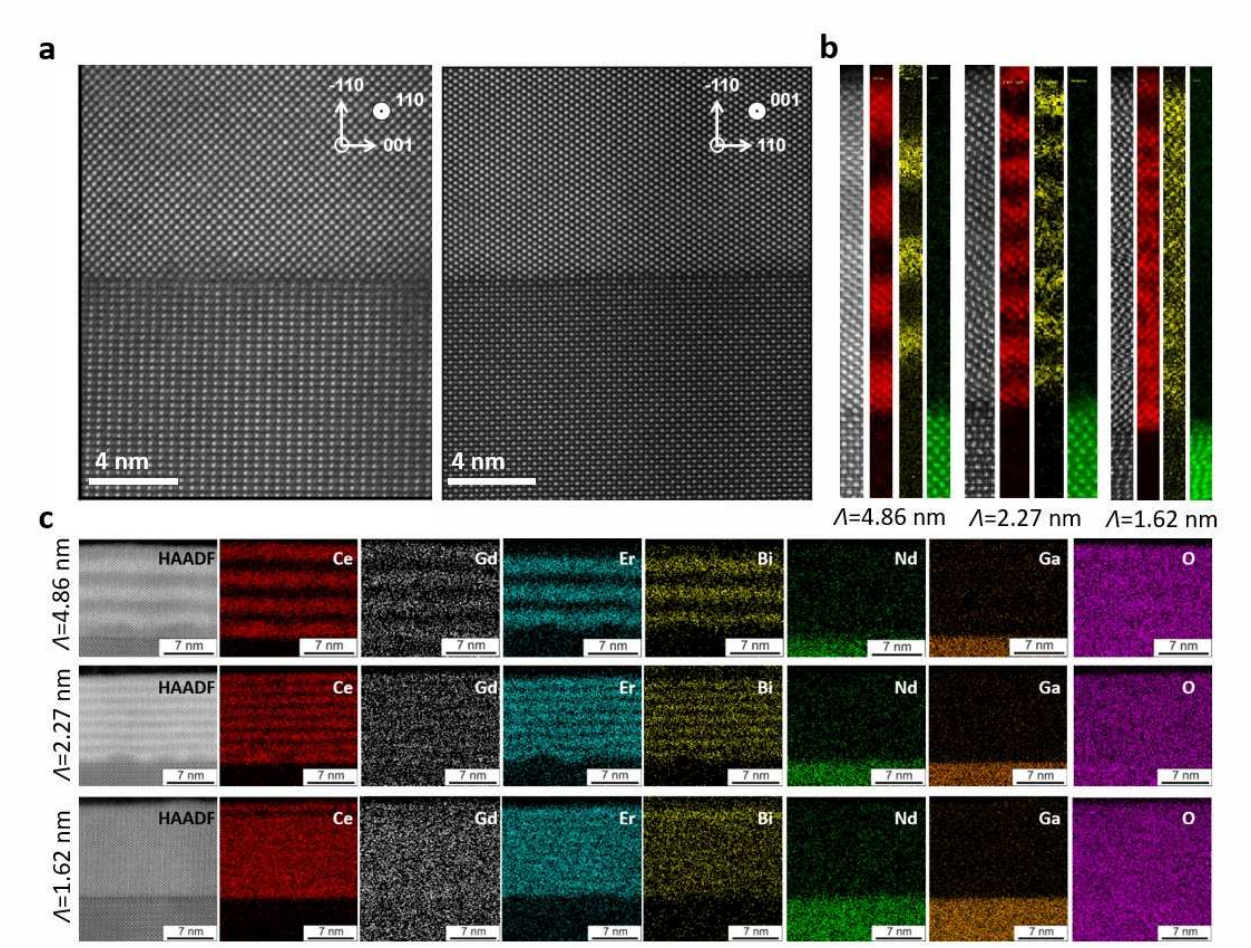

Extended Data Figure 1 | **STEM analysis of the heterostructures.** **a**. HAADF-STEM images for NGO/CGO[ESB/CGO]$_{10}$ viewed along the [110] and [001] directions of the substrate from left to right, respectively. **b**. STEM-EELS compositional maps. For each sample, the leftmost image is the HAADF signal acquired simultaneously with the EELS measurement, followed by cerium $M_{4,5}$ in red, erbium $M_{4,5}$ in yellow, and neodymium $M_{4,5}$ in green (colour code: Ce: red; Er: yellow, Nd: green). **c**. STEM-EDX compositional maps.

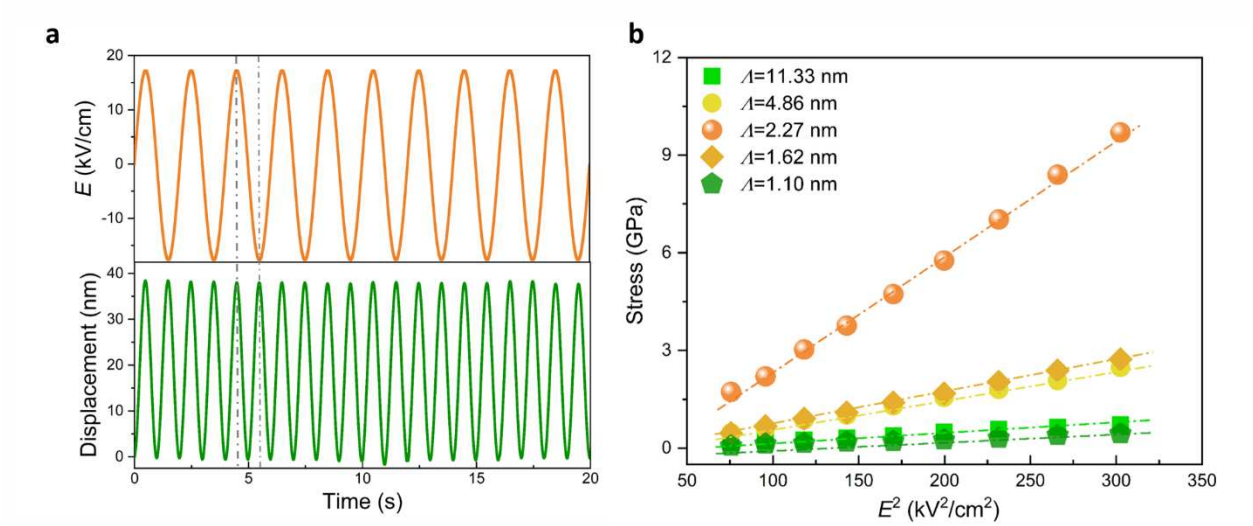

Extended Data Figure 2 | Electrostriction Measurements a. Electrostrictive response of NGO/CGO/[ESB/CGO]$_7$ under an alternating electric field. The strain developed at the second harmonic of the applied electric field. **b**. Field-induced stress as a function of the electrical field for NGO/CGO/[ESB/CGO]$_N$ measured at 1 Hz. The field-induced stress increases linearly with an increase in the squared electric field. No saturation was observed within the measured electric field range, regardless of the modulation length. The dash-dotted lines represent linear fittings of the measured results.

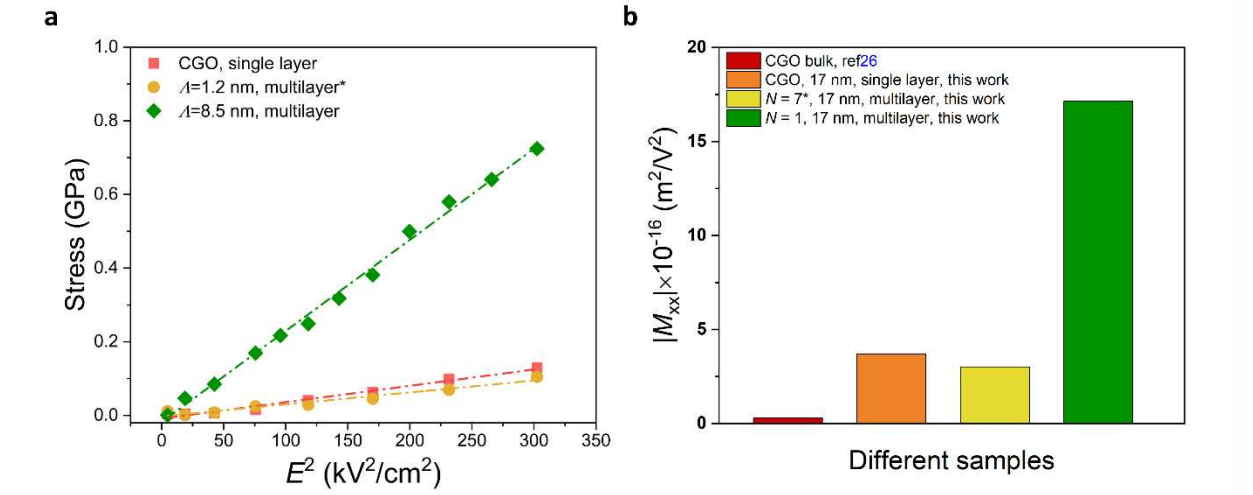

Extended Data Figure 3 | Electrostriction measurements for heterostructures with different stacking sequences. Comparison of electrostriction coefficients for thick CGO films and bulk materials Multilayer* denotes NGO(100)/ESB/CGO/…/CGO, where ESB was deposited as the first layer.

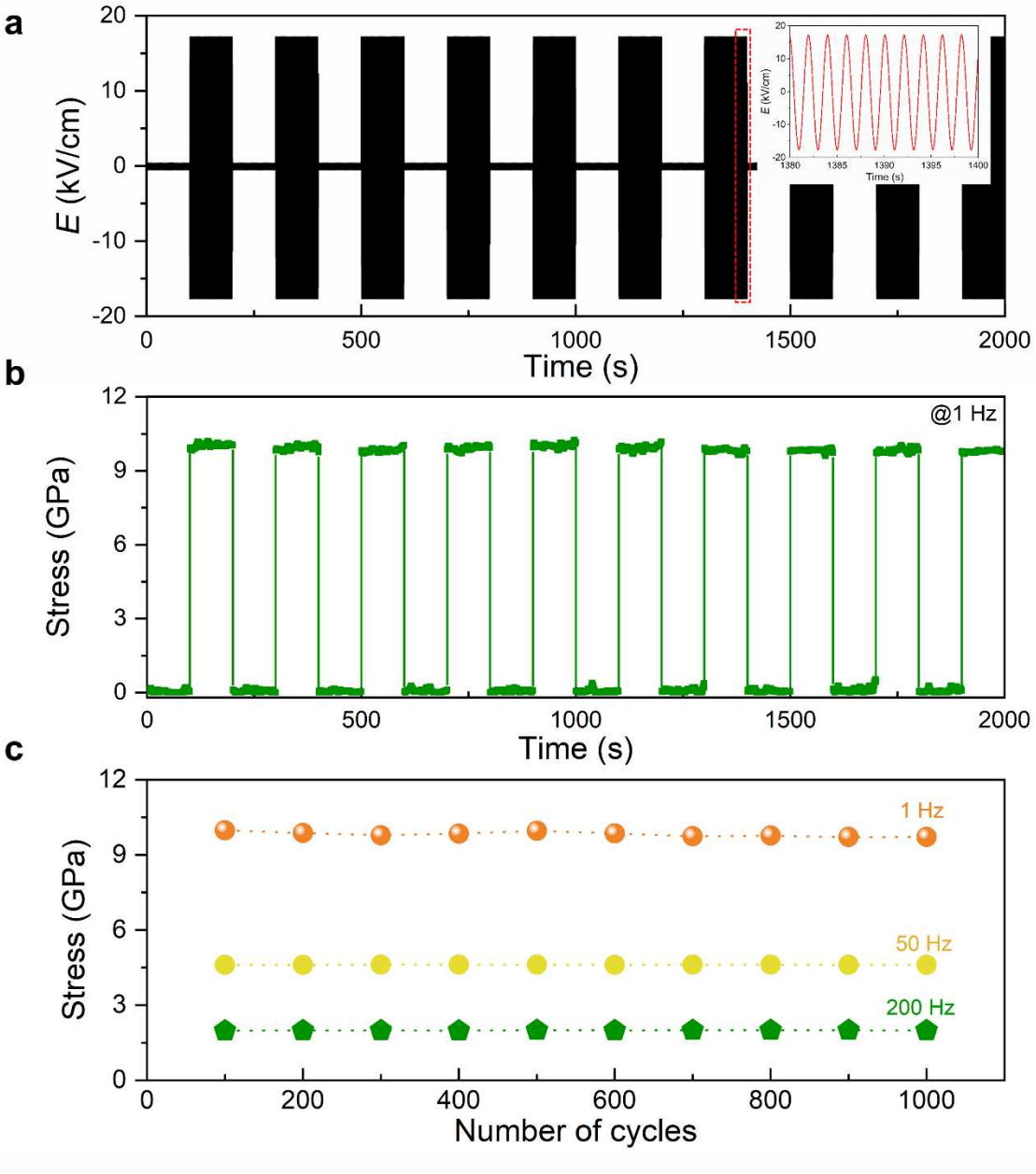

Extended Data Figure 4 | Fatigue measurements. Electromechanical response of NGO/CGO/$[ESB/CGO]_7$ as a function of time. **a**. Electric field. **b.** Electromechanical stress in response to an electric field at 1 Hz **c**. Electromechanical stress as a function of the measured cycles at 1, 50, and 200 Hz. All measurements were performed by applying a sinusoidal electric field with a constant amplitude of 17.4 kV/cm.

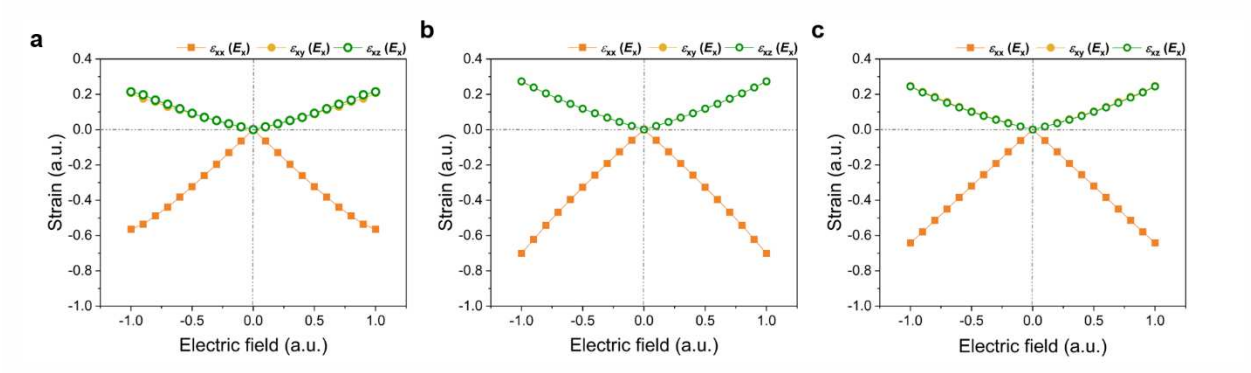

Extended Data Figure 5 | Calculated field-induced strains in different directions. **a**. CGO20; **b**. ESB20; **c**. heterostructure (Λ = 2.33 nm). An electrical field was applied along the (100)-crystallographic direction. All lattice parameters were allowed to relax during the application of the electrical field. ε_{xx}, ε_{xy}, and ε_{xz} denote the strain developed along *the X*-, *Y*-, and *Z*-axis, respectively when the electric field is applied along with the *X*-axis. The Cartesian axes *X*, *Y*, and *Z* correspond to the (100), (01-1) and (011) crystallographic directions, respectively. Note that the lattices of CGO20, ESB20, and the heterostructure exhibit similar deformation in response to an electric field, that is, contract along the (100)-crystallographic direction and expand along with the (011) and (01-1)-crystallographic directions.

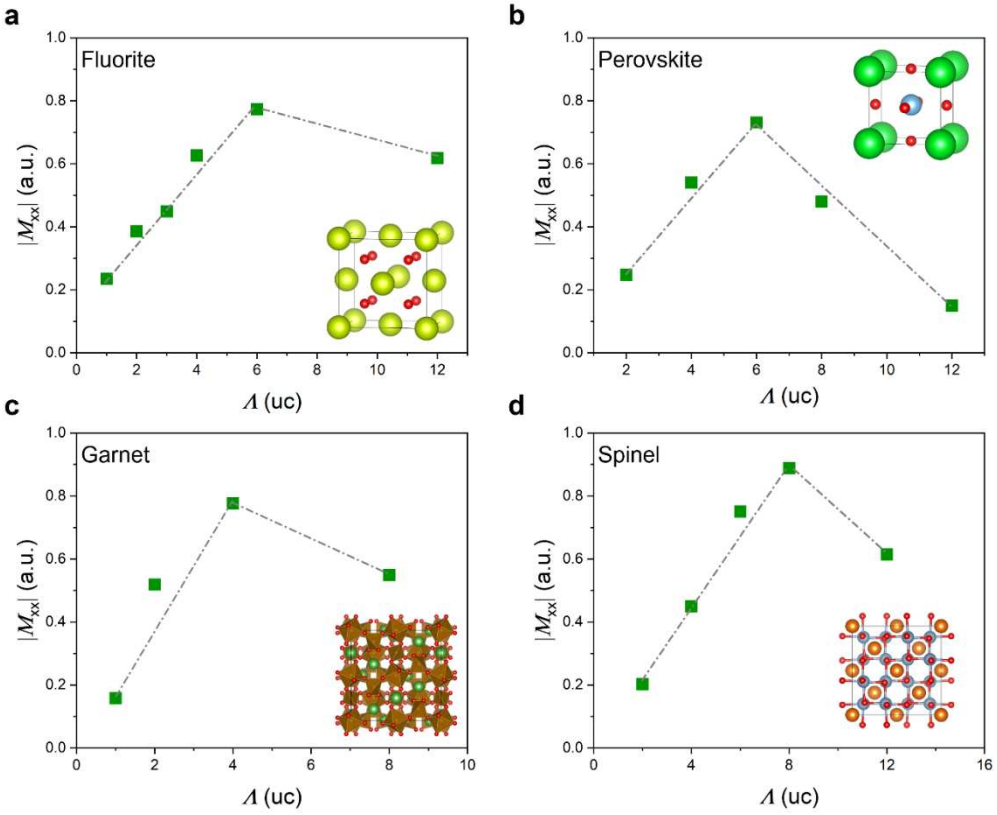

Extended Data Figure 6 | Electrostriction as a function modulation length for heterostructures with different crystal structures. **a**. fluorite: CGO20/YSZ8; **b**. perovskite: SFTO10/BYZO10; **c**. garnet: GGMO10/LSFO10; **d**. spinel: MGMO10/ZAZO10. The chemical formula for YSZ8, SFTO10, BYZO10, GGMO10, LSFO10, MGMO10 and ZAZO10 are $(Zr_{0.92}^{4+}Y_{0.08}^{3+})O_{1.96}^{2-}$, $Sr_{1.0}^{2+}(Fe_{0.1}^{3+}Ti_{0.9}^{4+})O_{2.95}^{2-}$, $Ba_{1.0}^{2+}(Y_{0.1}^{3+}Zr_{0.9}^{4+})O_{2.95}^{2-}$, $Gd_{3.0}^{3+}(Ga_{4.5}^{3+}Mg_{0.5}^{2+})O_{11.75}^{2-}$, $(La_{2.5}^{3+}Sr_{0.5}^{2+})Fe_{5.0}^{3+}O_{11.75}^{2-}$, $Mg_{1.0}^{2+}(Ga_{1.8}^{3+}Mg_{0.2}^{2+})O_{3.90}^{2-}$, $Zn_{1.0}^{2+}(Al_{1.8}^{3+}Zn_{0.2}^{2+})O_{3.90}^{2-}$, respectively. The defects are generated at random within the heterostructures. The insets schematically show the unit cell of the ideal structure. All the lattice parameters are allowed to relax during the application of the electrical field. Note that the optimal modulation length yielding maximized electrostriction coefficient (M_{xx}) is material dependent.

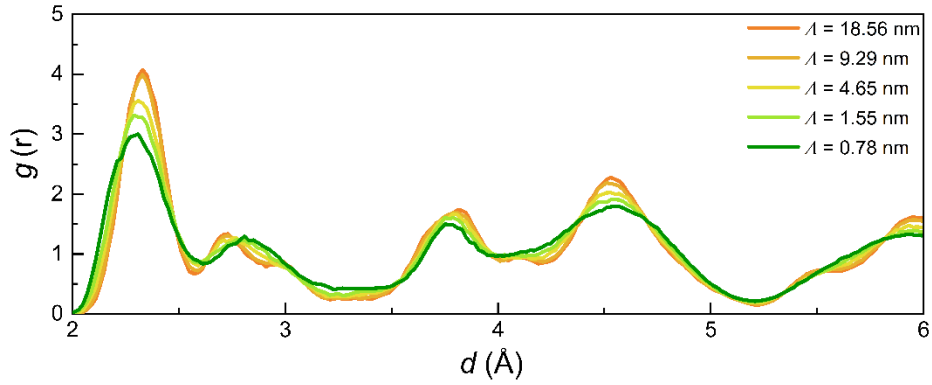

Extended Data Figure 7 | Ion distribution within the heterostructures. Radial distribution function of heterostructures as a function of modulation length (*Λ*). The first, second, and third peaks correspond to the cation–anion, anion–anion, and cation–cation distances, respectively. No electric field was applied.

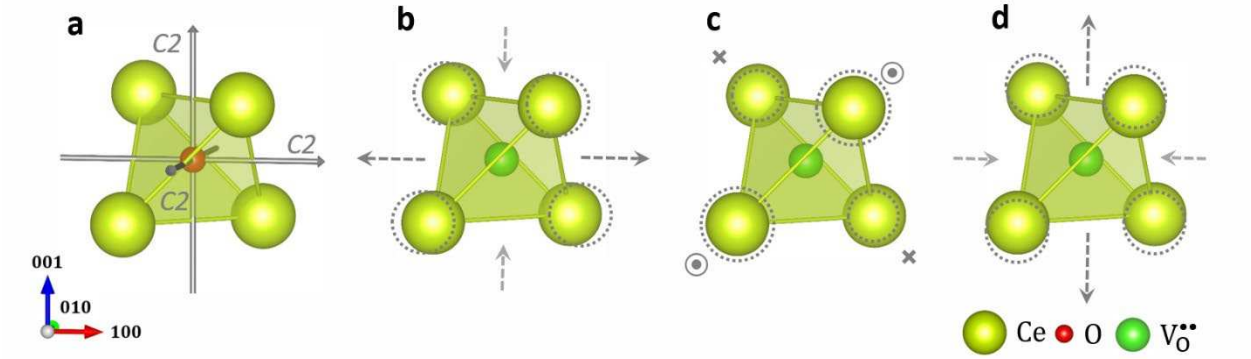

Extended Data Figure 8 | Mechanism of elastic dipole and electric dipole formation. a. An ideal tetrahedron with cations having equivalent distances and three *C2* symmetry axes present. Schematic illustration of the elastic dipole formation resulting from tetrahedral deformation along the **b**. (100), **c**. (010), and **d**. (001) directions. The off-site displacements of the cations result in local-symmetry breaking. Note that replacing one of the ions with Gd will result in a structure with three variants that are equivalent to the distortion of Ceria without Gd.

Supplementary Information

Atomically engineered interfaces yield extraordinary electrostriction

Haiwu Zhang[1*], Nini Pryds[1*], Daesung Park[2], Nicolas Gauquelin[3], Simone Santucci[1], Dennis V. Christensen[1], Daen Jannis[3], Dmitry Chezganov[3], Rata Diana[4], Andrea R. Insinga[1], Ivano E. Castelli[1], Johan Verbeeck[3], Igor Lubomirsky[5], Dragan Damjanovic[2], and Vincenzo Esposito[1*]

1. Cross-section analysis by HAADF-TEM

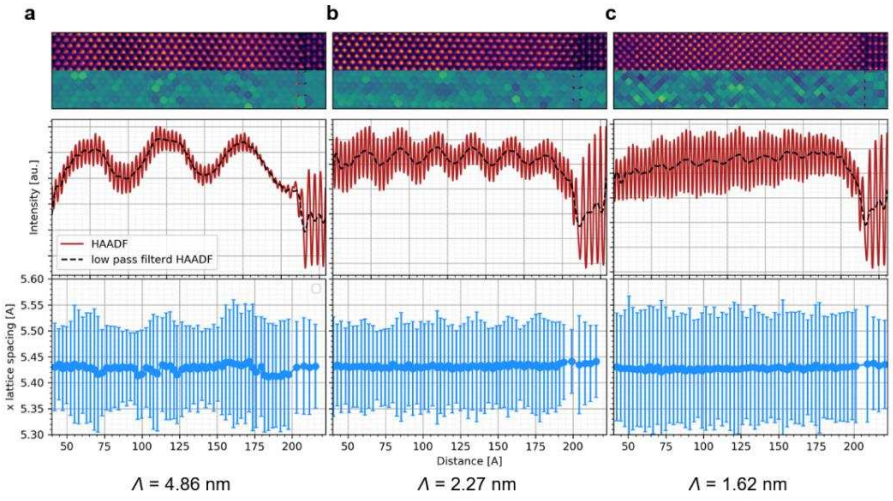

Supplementary Fig. 1 | HAADF-TEM analysis along the cross-section of the heterostructures. a. Λ = 4.86 nm. **b**. Λ = 2.27 nm. **c**. Λ = 1.62 nm. Note that the in-plane lattice parameters of CGO/[ESB/CGO]$_N$ are constant along the cross-section of the heterostructures (blue data points).

2. Free energy by atomic-scale simulations

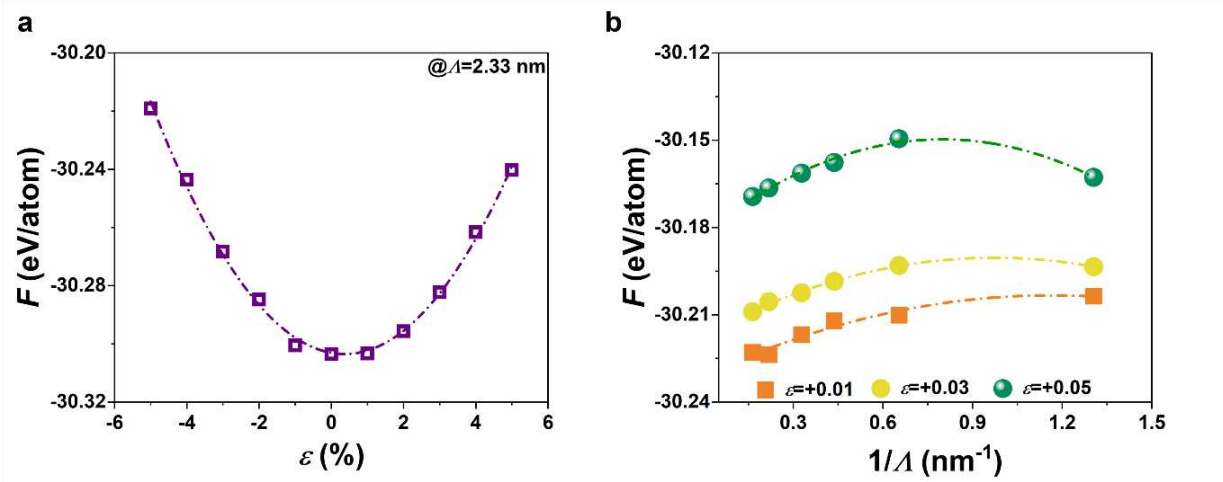

Supplementary Fig. 2| Helmholtz free energy as a function of modulation length and biaxial strain. **a**. Free energy (F) of heterostructure with a modulation length (Λ) of 2.33 nm. **b**. Free energy as a function of Λ for different biaxial strains (ε). The simulations were performed by fixing the in-plane lattice parameters, allowing the out-of-plane lattice parameters to change.

Supplementary Fig. 2a shows the Helmholtz free energy (F) of heterostructure with a modulation length (Λ) of 2.33 nm. The value of F increases with the increase of the biaxial strain. The calculated F for different strain values (without applying an electric field) exhibits a maximum as a function of Λ (Supplementary Fig. 2b), which can be attributed to the lattice distortions caused by the interfacial strain at the CGO/ESB interfaces.

3. Electrostriction measurement

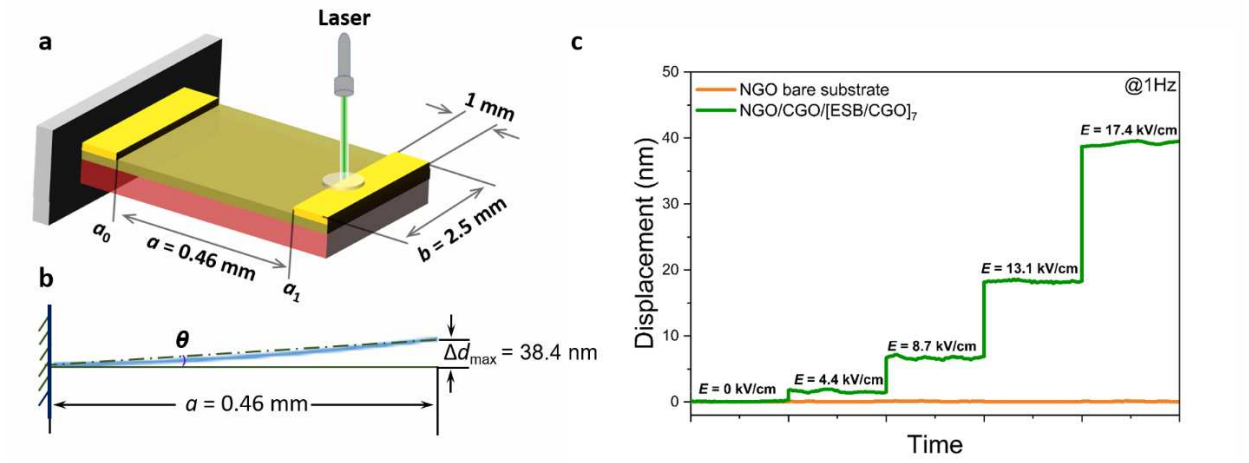

Supplementary Fig. 3 | Electrostriction measurement. a. Schematic illustration of the geometry of the cantilever. The displacement along the out-of-plane direction is measured as a function of time under an electric field. **b**. Schematic illustration of the deformation of the cantilever. The blue line denotes the curvature. **c**. Comparison of the displacements of bare $NGO_{(100)}$ substrate with $NGO/CGO/[ESB/CGO]_N$ as a function of electric field using the planar electrode configuration.

Supplementary Fig. 3a schematically illustrates the geometry of the cantilever with a planar electrode configuration, with the two electrodes placed on top of the thin films in parallel. This configuration does not require the bottom electrode, thus facilitating the choice of a substrate with the desired lattice mismatch (and therefore, biaxial strain).[38] The displacements (Δd) that respond to the electric field at the free end of the cantilever (a_1) were measured. This configuration yields the longitudinal electrostriction coefficient (*i.e.*, M_{33}).[38] However, M_{xx} is used for ease of comparison with results taken from the literature. The distance (a) between the two electrodes was 0.46 mm, width (b) was 2.5 mm, and thickness of the NGO substrate was 0.1 mm.

The induced curvature (Δk) is calculated using $\Delta k = 2\Delta d/(a^2)$.[39] Subsequently, the in-plane stress is calculated using the well-known Stoney formula[39]

$$\Delta\sigma = \frac{Y_{sub}}{1 - v_{sub}} \frac{d_{sub}^2}{6t_{film}} \Delta k \qquad 1$$

where Y_{sub} is Young's modulus, v_{sub} is the Poisson ratio, and d_{sub} and d_{film} are the thicknesses of the substrate and film, respectively.

Then, M_{xx} is obtained by linearly fitting the stress ($\Delta\sigma$) against the electric field squared by:

$$M_{xx} = \frac{\Delta\sigma}{E^2 \cdot Y_{film}} \quad (2)$$

where Y_{film} is the Young's modulus of the heterostructures, which is taken to be the weighted average of CGO and ESB. The Young's modulus (Poisson ration) for NGO, CGO and ESB are 200.97(0.29)[40], 200(0.33)[41], and 72.8(0.39)[42], respectively.

For NGO/CGO/[ESB/CGO]$_7$, the maximum displacement is 38.4 nm under the highest electric field (V/a = 17.4 kV/cm) at 1 Hz. This configuration yields a deformation of $\Delta d_{max}/a$ = 38.4 nm/0.46 mm = 8.35×10^{-5} << 1% (Supplementary Fig. 3b), corresponding to an angle change of 0.00478295°; such a small angle change indicates that the "bending" of the cantilever can be neglected. Supplementary Fig. 3c shows the displacements of the bare NGO$_{(100)}$ substrate with the planar electrode configuration; the NGO was not electrostrictive-active. Thus, the contributions associated with high electric fields, such as polarisation or electrostatic forces (*i.e.,* Maxwell stress tensor), can be neglected. This assumption is consistent with the results of Fig. 1c discussed in the main text with the same planar electrode configuration, M_{xx} increases by approximately two orders of magnitude from NGO/CGO to NGO/CGO/[ESB/CGO]$_7$, which suggests that the variation of the thin film dominates the electromechanical response.

4. Electric field distribution by finite element simulations

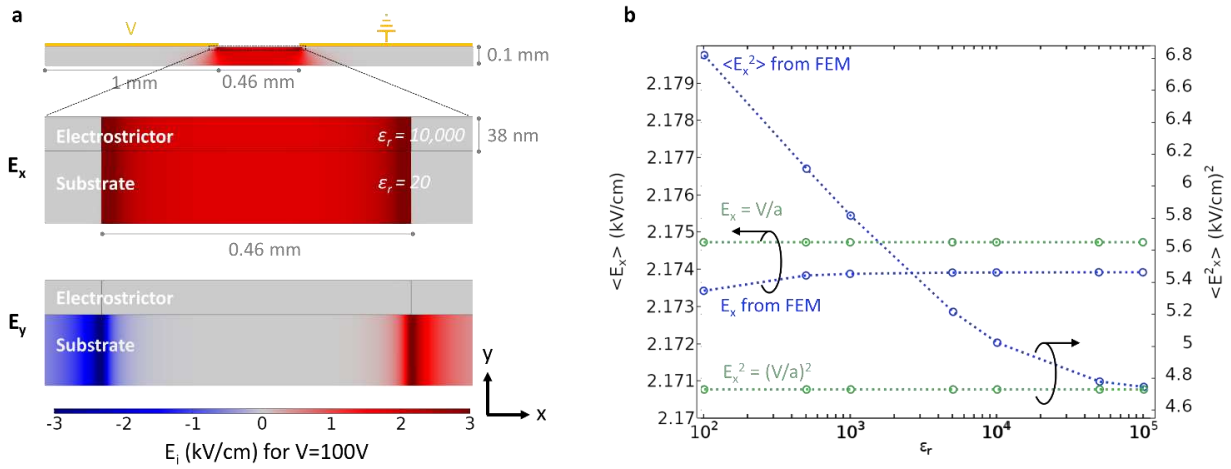

Supplementary Fig. 4 | Electric field distribution by finite element simulations. a. Distribution of the *X*- and *Y*-components of the electric field (E_x and E_y) in the electrostrictive cantilever and NGO substrate when an electrostatic potential of $V = 100$ V is applied. **b** Average of the electric field and squared electric field as a function of the dielectric constant of the thin film. The average is calculated in the 0.46 mm × 38 nm region of the electrostrictive film between the electrodes and compared to the naïve prediction where $E_x = V/a$. Note that the dielectric displacement field is channelled by the high dielectric constant materials, i.e., CGO.

Finite element modelling (FEM) was performed to account for the electric field distribution, according to the procedure described by Nigon *et al.*[38]. Here, the electric field distribution was calculated using a 2D model of the cantilever geometry in Supplementary Fig. 3a. A grounded electrode and a biased electrode were placed on top of the thin film deposited on the NGO substrate. The cantilever was further surrounded by air at the top and bottom. The deposited superlattice was modelled as a single dielectric layer. A custom mesh was created to account for the high aspect ratio of the thin films. The average electric field in the thin film was invariant to its thickness in the probed range ($38 \leq d_{film} \leq 80$ nm). The electric field distribution is shown in Supplementary Fig. 4a; E_x is the dominant component in the film, which is consistent with previous studies.[38, 43]. The electric field was fairly constant in the majority of the electrostrictor ($E_x = 0$ below the electrodes and $E_x \sim V/a$ between the electrodes), with the only significant inhomogeneities observed close to the edge of the electrodes; E_x increased from 0 below the electrodes, encountered a peak, and decreased to a constant value. The average of E_x and E_x^2 as a function of the dielectric constant of the electrostrictor is shown in Supplementary Fig. 4b. For all probed dielectric constants, the average E_x can be approximated well by $E_x \approx V/a$. However, for low dielectric constants, the peak in E_x close to the electrode edge increases, increasing the average of E_x^2. However, the thinner the film with respect to the electrode distance, the lower

the impact of the region close to the electrode. The geometry and high dielectric constant of the electrostrictive heterostructure used here ensure that $E_x \approx V/a$ and $E_x^2 \approx (V/a)^2$ are fair approximations and are used in the following for convenience.

5. Atomic-scale simulations

a

M-O^{2-}	A/eV	ρ/Å	C/eV Å^6	ref
Ce^{4+}-O^{2-}	1809.68	0.3547	20.40	44
Gd^{3+}-O^{2-}	1885.75	0.3399	20.34	44
Bi^{3+}-O^{2-}	2496.91	0.3305	18.25	This work
Er^{3+}-O^{2-}	1719.91	0.3389	17.55	45
O^{2-}-O^{2-}	9547.96	0.2192	32.0	44, 45

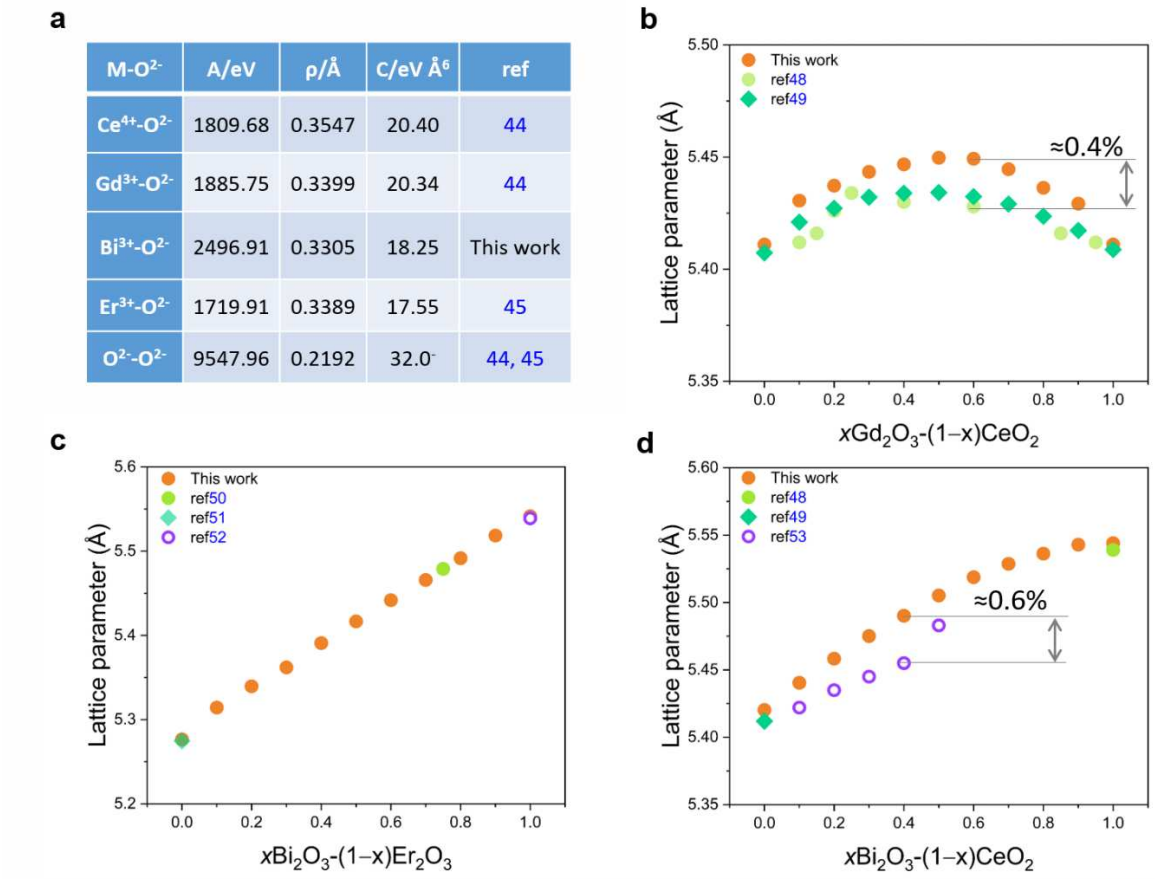

Supplementary Fig. 5 | Potential parameters and ground-state structural properties. **a**. Table showing the short-range Buckingham potential parameters. More details about the potential parameters for other systems shown in Extended Data Figure 6 were taken from refs. 46 and 47. **b**, **c,** and **d**, comparison of calculated and experimental lattice parameters for xGd_2O_3-$(1–x)CeO_2$ (**b**), xEr_2O_3-$(1–x)Bi_2O_3$ (**c**), and xBi_2O_3-$(1–x)CeO_2$ (**d**). The maximum difference between the calculated values and experimental values is ~0.4% for xGd_2O_3-$(1–x)CeO_2$ and ~0.6% for xBi_2O_3-$(1–x)CeO_2$. The lattice parameters for xGd_2O_3-$(1–x)CeO_2$ were taken from refs 48, 49. The lattice parameters for Bi_2O_3, Er_2O_3 and $Er_{0.8}Bi_{1.2}O_3$ were taken from Ref 50, 51, and 52. The lattice parameters for $xBi_2O_{3-(1-x)}CeO_2$ were taken from Ref 53 (open circles).

The Buckingham potential parameters for ceria employed in the current study were developed by Minervini *et al.*[44] They have already been validated extensively and can describe the lattice parameter, elastic constants, thermal expansion coefficient, heat capacity, defect formation energies, and defect-dislocation interactions.[45]

The potential parameters are adequate to model the nonlinear variation of the CGO lattice parameter as a function of the dopant concentration (Supplementary Fig. 5b). Supplementary Fig. 5c and d further show that the calculated lattice

parameters of $xBi_2O_{3-(1-x)}Er_2O_3$ and $xBi_2O_{3-(1-x)}CeO_2$ are consistent with previous experimental results for δ-Bi_2O_3, Er_2O_3, and their solid solutions.[48-53] The pressure is maintained at 1.01325 bar to simulate such solid solutions.

The steps for the molecular dynamics simulations are listed below. 1) Construct the $(100) \times (0\bar{1}1) \times (011)$-orientated heterostructures with various modulation lengths; 2) introduce the dopants and oxygen vacancies at random; 3) apply biaxial strains by adjusting the in-plane lattice parameters to specific values; 4) equilibrate at 2400 K for 600 ps, followed by another equilibration at 300 K for 300 ps; 5) turn on the electrical field along the (100)-crystallographic direction at 300 K and extract the optimised structures after 100 ps.

Large supercells were used to account for the various possible distributions of the point defects within the heterostructures: $10 \times 8\sqrt{2} \times 24\sqrt{2}$ (41472 atoms) and $16 \times 12\sqrt{2} \times 12\sqrt{2}$ (49768 atoms) were used to model the interlayer interaction (Fig. 3) and the electrostriction coefficient (Fig. 4b), respectively. The position of the cationic planes was determined by averaging the position of the cations within each layer, based on which cationic interplanar distance (d_C) was calculated. The chemical formulae were $Ce_{6144}Gd_{1536}O_{14592}/Bi_{6144}Er_{1536}O_{11520}$, and $Ce_{7376}Gd_{1840}O_{17512}/Bi_{7376}Er_{1840}O_{13824}$, corresponding to the experimental compositions of $Ce_{0.8}Gd_{0.2}O_{1.9}$ and $Er_{0.4}Bi_{1.6}O_3$, respectively. Thus, various distributions of defects and their responses to the electric field were included in the model and were captured by the generated dipoles. The pressure was maintained at 0.0 bar for the simulation of heterostructures.

6. Phenomenological simulations.

To evaluate the effect of the volumetric strain observed experimentally, we investigate the electrostriction as a function of volumetric strain ($\Delta V/V$) by considering a model based on the energy of elastic and electric dipoles. This model considers an ensemble of elastic dipoles, where the elastic dipole moment is rigidly connected to an electric dipole. We assume that the elastic-electric dipole interacts with an initial strain field and external electric field by changing its orientation in space. The equilibrium orientation is the one that minimises the sum of the elastic and electric interaction energies.

We denote the electric dipole vector and elastic dipole tensor by $\boldsymbol{p}$ and $\overline{\overline{\Sigma}}$, respectively, and their components by p_j and Σ_{ij}, respectively. We assume that the electric and elastic dipoles rotate together. This assumption is consistent with the recent analysis of electrical and electrical dipoles formation in oxygen defective cerium oxide proposed by Das *et al*.[29] Denoting the components of the rotation matrix as R_{ij}, we have:

$$\begin{cases} p'_i = R_{ij} p_j \\ \Sigma'_{ij} = R_{ik} R_{jh} \Sigma_{kh} \end{cases} \quad (3)$$

where the Einstein summation convention is adopted. The rotation is parametrised by three angles, $\{\alpha_1, \alpha_2, \alpha_3\}$, for example, the Euler angles. We minimise the total energy of the system with respect to these angles. The total energy is

$$E_{\text{total}} = E_{\text{elastic}} + E_{\text{electric}} \quad (4)$$

where E_{elastic} and E_{electric} are the elastic and electric contributions, respectively.

Written in terms of their components, the interaction energy between the elastic point dipole Σ'_{ij} and the strain field ε_{ij} is:[54]

$$E_{\text{elastic}} = -\Sigma'_{ij} \varepsilon_{ij} \quad (5)$$

Likewise, the interaction energy between the electric point-dipole p'_i and the external electric field E_i is:

$$E_{\text{electric}} = -p'_i E_i \quad (6)$$

The dipoles will assume the orientation associated with the minimum total energy, which corresponds to minimising E_{total} with respect to the angles $\{\alpha_1, \alpha_2, \alpha_3\}$. This configuration is illustrated in Supplementary Figure 6.

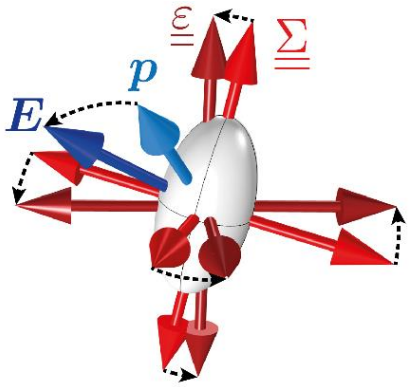

Supplementary information Fig. 6 | Schematic illustration of the coupling between electric and elastic dipoles. The symbols, $\bar{\bar{\Sigma}}$, p, $\bar{\bar{\varepsilon}}$, and E denote elastic dipole, electric dipole, strain field and electric field, respectively. Note that the external electric field polarises the electric dipole. The reorientation of the electric dipole is accompanied by the reorientation of the elastic dipole, which generates field-induced strain.

We thus obtain the electric dipole $\boldsymbol{p}_{\mathrm{eq}}$ and elastic dipole $\bar{\bar{\Sigma}}_{\mathrm{eq}}$ corresponding to the minimum energy equilibrium orientation. We then consider the average electric polarisation $\boldsymbol{P}$ and average mechanical stress $\bar{\bar{\sigma}}$ associated with the electric-elastic dipoles:

$$\begin{cases} \boldsymbol{P} = \rho_{\mathrm{dipoles}}\, \boldsymbol{p}_{\mathrm{eq}} \\ \bar{\bar{\sigma}} = \rho_{\mathrm{dipoles}}\, \bar{\bar{\Sigma}}_{\mathrm{eq}} \end{cases} \tag{7}$$

where ρ_{dipoles} is the volume density of dipoles (i.e. number of dipoles per unit volume). We now compute the electric susceptibility tensor $\bar{\bar{\chi}}$ from the relation

$$\boldsymbol{P} = \epsilon_0 \bar{\bar{\chi}} \boldsymbol{E} \tag{8}$$

where ϵ_0 denotes the vacuum permittivity. Here, since the electric field $\boldsymbol{E}$ has been applied along the x direction, we will obtain the first column of $\bar{\bar{\chi}}$ (which is a symmetric tensor). In order to obtain the electrostrictive coefficients from $\bar{\bar{\chi}}$ and $\bar{\bar{\sigma}}$, we need to apply the following relation[55, 56]:

$$M_{ijkl} = \left(\frac{\epsilon_0}{2}\right)\left(\frac{d\chi_{ij}}{d\sigma_{kl}}\right)_E \tag{9}$$

where the subscript E indicates that the derivative must be evaluated for constant electric field E. To apply the previous equation, we must evaluate the relation between stress and electrical susceptibility while varying the relative strength between the elastic and electric interaction. Therefore, we evaluate the variation of $\bar{\bar{\chi}}$ and $\bar{\bar{\sigma}}$ by performing a re-scaling by a factor γ of the original elastic dipole given as input:

$$\bar{\bar{\Sigma}} \longrightarrow \gamma \bar{\bar{\Sigma}} \tag{10}$$

This re-scaling corresponds to changing the strength of the elastic dipole. We now repeat the same procedure for calculating $\bar{\bar{\chi}}$ and $\bar{\bar{\sigma}}$. Since the elastic energy is proportional to γ, the re-scaling changes the trade-off between the elastic and electric energy, therefore changing the solution. In this way, we obtain the following solutions as a function of γ:

$$\bar{\bar{\chi}} = \bar{\bar{\chi}}(\gamma) \text{ and } \bar{\bar{\sigma}} = \bar{\bar{\sigma}}(\gamma) \qquad 11$$

From the resulting curve $\chi_{xx}(\sigma_{xx})$ we consider the limit for which the electrical interaction is dominating, i.e. $\gamma \longrightarrow 0$, and evaluate the derivative in this limit. Since we are interested in the coefficient M_{xxxx}, we will use the following relation:

$$M_{xxxx} = \left(\frac{\epsilon_0}{2}\right)\left(\frac{d\chi_{xx}}{d\sigma_{xx}}\right)_E \qquad 11$$

The electrostrictive coefficient M_{xxxx} (shortened as M_{xx}) is then calculated in this way for different values of the out of plane strain ε_{zz}, corresponding to different values of the volumetric strain ($\Delta V/V$) to generate a relation between M_{xx} and ($\Delta V/V$).

As indicated in ref 29, we assume the following expression for the elastic dipole tensor:

$$\bar{\bar{\Sigma}} = \begin{pmatrix} -9.633 & 0.001 & 0.001 \\ 0.001 & -9.633 & 1.734 \\ 0.001 & 1.734 & -9.633 \end{pmatrix}$$

Moreover, we assume the following inputs:

$$\bar{\bar{\varepsilon}} = \begin{pmatrix} 1\% & 0 & 0 \\ 0 & 1\% & 0 \\ 0 & 0 & \varepsilon_{zz} \end{pmatrix}; \boldsymbol{E} = \begin{pmatrix} 1 \\ 0 \\ 0 \end{pmatrix}; \boldsymbol{p} = 10^{-5}\begin{pmatrix} 0 \\ 2 \\ 0 \end{pmatrix};$$

The resulting curve of the electrostrictive coefficient M_{xx} as a function of $\Delta V/V$ is shown in Fig. 4a

It is important to stress that when the density of defects is sufficiently low (as it is in the case considered here), it is a justifiable assumption to consider the dipoles as independent. Instead, when the density of defects is high, it is necessary also to include the dipole-dipole nearest-neighbour interaction terms. The elastic and electric nearest-neighbour interaction energies have a form analogous to that of the Ising/Heisenberg model, and they can be expressed as:

$$E_{elastic-elastic} = J_{elastic} \sum_{\langle h,k \rangle} \Sigma_{ij}^h \, \Sigma_{ij}^k \qquad 13$$

$$E_{electric-electric} = J_{electric} \sum_{\langle h,k \rangle} \mathrm{p}_i^h \, \mathrm{p}_i^k \qquad 14$$

Here $J_{elastic}$ and $J_{electric}$ are the interaction strengths coefficients, the superscript indexes h and k indicate specific dipole locations in the lattice, and the notation $\langle h, k \rangle$ indicates that the summation only runs among nearest-neighbour dipoles. Depending on the signs of $J_{elastic}$ and $J_{electric}$, these interaction terms promote aligned or anti-aligned configurations.

However, our simple non-interacting dipoles model can produce results that agree with the trend observed experimentally and provide an intuitive explanation for the mechanism behind the enhanced electrostriction. Hence, we decided not to include these terms in our calculations, which is a realistic assumption given the low spatial density of defects.

References

38. Nigon, R., Raeder, T. M., Muralt, P. Characterization methodology for lead zirconate titanate thin films with interdigitated electrode structures, *J. Appl. Phys*. **121**, 204101 (2017).

39. Mazzalai, A. et al, Characterisation and fatigue of the converse piezoelectric effect in PZT films for MEMS applications, *J. Microelectromech. Syst.* **24**, 831-838 (2015).

40. https://materialsproject.org/materials/mp-3196/.

41. Morales, M. et al, Mechanical properties at the nanometer scale of GDC and YSZ used as electrolytes for solid oxide fuel cells, *Acta Mater*. **58**, 2504-2509 (2010).

42. http://progs.coudert.name/elate/mp?query=mp-22891.

43. Nguyen, C. H. et al, Probing-models for interdigitated electrode systems with ferroelectric thin films, *J. Phys. D: Appl. Phys*. **51** (2018).

44. Minervini, L., Grimes, R. W., Sickafus, K. E. Disorder in pyrochlore oxides, *J. Am. Ceram. Soc*. **83**, 1873-1878 (2000).

45. Vyas, S., Grimes, R. W., Gay, D. H., Rohl, A. L. Structure, stability and morphology of stoichiometric ceria crystallites, *Faraday Trans*. **94**, 427-434 (1998).

46. De Souza, R. A. Maier, J. A computational study of cation defects in $LaGaO_3$, *Phys. Chem. Chem. Phys*. **5**, 740-

748 (2003).

47. Zacate, M. O. Grimes, R. W. Predicted calcium titanate solution mechanisms in calcium alumioferrite and related phases, *J. Mater. Sci*. **35**, 3727-3732 (2000).

48. Kossoy, A. et al. Evolution of the local structure at the phase transition in CeO_2-Gd_2O_3 solid solutions, *Phys. Rev. B*. **87**, 054101 (2013).

49. Artini, C., et al, Structural characterisation of the CeO_2/Gd_2O_3 mixed system by synchrotron X-ray diffraction, *J. Solid State Chem*. **190**, 24-28 (2012).

50. Battle, P. D., Catlow, C. R. A., Moroney, L. M. Structural and dynamical studies of δ-Bi_2O_3 oxide-ion conductors II, *J. Solid State Chem*. **67**, 42-50 (1987).

51. Heiba, Z. K., Mohamed, M. B., Fuess, H. Effect of Mn doping on structural and magnetic susceptibility of C-type rare earth Nano oxides $Er_{2-x}Mn_xO_3$, *Mater. Res. Bull*. **47**, 4278-4282 (2012).

52. Begemann, B., Jansen, M. Bi_4O_7, das erste definierte binÄre Bismut(III, V)-Oxid. *Less Comm. Metal*. **156**, 123-135 (1989).

53. Sardar, K. et al. Nanocrystalline cerium-bismuth oxides: Synthesis, structural characterisation, and redox properties, *Chem. Mater*. **22**, 6191-6201 (2010).

54. Dudarev, S. L., Ma, P.-W. Elastic fields, dipole tensors, and interaction between self-interstitial atom defects in bcc transition metals, *Phys. Rev. Materials*. **2**, 033602 (2018).

55. Newnham, R. E., Sundar, V., Yimnirun, R., Su, J., Zhang, Q. M. Electrostriction: Nonlinear Electromechanical Coupling in Solid Dielectrics, *J. Phys. Chem. B*. **101**, 10141-10150 (1997).

56. Eury, S., et al. Converse electrostriction in polymers and composites, *Mater. Chem. Phys*. **61**, 18-23 (1999).